NTNU
Norwegian University of
Science and Technology

Estimation of Aerodynamic Forces on a Railway Contact Wire and Their Effect on Galloping Instability

Wind Tunnel Testing of an AC-120 Contact Wire

Andrea Rokke Elvebakken

Mechanical Engineering
Submission date: February 2018
Supervisor: Ole Andre Øiseth, KT

Norwegian University of Science and Technology
Department of Structural Engineering

Sammendrag

Målet med denne masteroppgaven var å bestemme de statiske aerodynamiske kreftene på en kontaktledning, presentert som statiske koeffisienter og i form av Strouhalnummeret. De statiske koeffisientene ble brukt i en galopping-analyse på en Finite Element-modell av en jernbanestrekning i Norge.

Den første fasen av prosjektet var å designe modellen. To forskjellige tverrsnitt ble vurdert; oppskalering av 5 og 10 ble sammenlignet. Beslutningen baserte seg på stabilitetsberegninger for vindtunneltesting og estimering av kreftene som skulle måles. Modellen som ble valgt var en AC-120 kontaktledning skalert 5:1.

Den andre fasen var å bygge modellen. Kontaktledningsdelen av modellen skulle egentlig lages i plastskum, men skaleringen tillot ikke dette. Modellen ble til slutt 3D-printet av Sintef Ocean AS i Trondheim. 3D-printene ble montert rundt et aluminiumrør i laben ved Institutt for konstruksjonsteknikk. Sprekkene i modellen ble tettet med lim, og spraymaling ble brukt som overflatebehandling.

Den tredje fasen var vindtunneltestingen som ble utført i Strømningsteknisk laboratorium ved Institutt for Energi og Prosessteknikk, NTNU. Tre vindhastigheter ble testet; 4, 6 og 10 m/s. Hastighetene ble testet ved angrepsvinkler fra -75 til 75°. Modellen ble rotert i en rig designet av Institutt for Konstruksjonsteknikk. Egenfrekvensen til modellen ble også estimert.

Den siste fasen besto av behandling av resultatene fra vindtunnelen samt utførelse av galopping-analysen. De statiske koeffisientene ble plottet mot angrepsvinkel og Reynoldstall. Resultatene ble også presentert i form av Glauert-Den Hartog stabilitetskriteriet for galopping. Strouhalnummeret ble bestemt fra en tidsserie med økende vindhastighet fra 0 til 10 m/s. Gallopping-analysen ble utført på to forskjellige måter med forskjellige utgangspunkt.

De statiske koeffisientene var avhengig av Reynolds tall og angrepsvinkel. Økende vindhastighet reduserte dragkoeffisienten. Absoluttverdien til løftkoeffisienten økte stort sett med økende vindhastighet. Momentkoeffisienten økte med økende vindhastighet for negative angrepsvinkler, og motsatt for positive vinkler. Stabilitetskriteriet ga mulige ustabile angrepsvinkler ved alle vindhastighetene som ble testet. De ustabile vinklene inkluderte vinkler fra -74 til -57°, noen vinkler rundt 0°, noen vinkler mellom 16 og 26°, og noen vinkler fra 55 til 64°. Strouhalnummeret ble estimert til 0.194. Galloping-analysen ga mange kritiske angrepsvinkler kombinert med kritiske vindhastigheter. De fleste vinklene stemte overens med stabilitetskriteriet, men en av analysene ga vinkler som ikke gjorde det. Mange av de kritiske modeformene var vertikale. Noen av de større angrepsvinklene ga utslag i både vertikal- og horisontalretningen. Det er altså muligheter for ustabile vibrasjoner på jernbanestrekningen, men kritisk angrepsvinkel og vindhastighet må skje samtidig. En begrensning for analysen var at den ene hastigheten i vindtunnelen, som ble brukt i analysen, ga virvelavløsninger på modellen. En annen svakhet ved analysen var at alle elementene i kontakledningsanlegget ble beskrevet med koeffisientene til kontaktledningen.

Abstract

The objective of this master thesis was to determine the static aerodynamic forces on a contact wire, presented as static coefficients and the Strouhal number. The static coefficients were used in a galloping analysis on a Finite Element model of a real life catenary system in Norway.

The first phase of the project was to determine the design of the wind tunnel model. Two different cross-sections were considered; up-scaling of 5 and 10 were compared. The decision was based on stability calculations for wind tunnel testing and estimations of force measurements. The final design was an AC-120 contact wire scaled 5:1.

The second phase was to build the model. The original idea was to make the contact wire cross-section with a plastic foam material, but the scaling didn't allow for the right processing to this material. So, the contact wire shape was 3D-printed by Sintef Ocean AS in Trondheim. The 3D-print was assembled around an aluminum pipe in the laboratory at the Department of Structural Engineering. The cracks in the model were sealed with glue, and spray paint was used as surface treatment to obtain constant surface properties.

The third phase was the wind tunnel testing which was performed in the Fluid Mechanics Laboratory at the Department of Energy and Process Engineering, NTNU Gløshaugen. Three wind velocities were tested; 4, 6 and 10 m/s. The velocities were tested at angles of attack from -75 to 75°. The flow angles were demonstrated by rotating the model in a rig designed by the Department of Structural Engineering. A natural frequency test was also performed.

The final phase consisted of processing the wind tunnel results as well as performing the galloping analysis. The static coefficients were plotted versus angle of attack and Reynolds number. The results were also presented in the form of the Glauert-Den Hartog stability criterion for galloping. The Strouhal number was determined from a time series with wind velocities from zero to 10 m/s. Two approaches were made to the galloping analysis.

The static coefficients were dependent on Reynolds number and angle of attack. The drag coefficient decreased with increasing velocity. The magnitude of the lift coefficient generally increased with increasing velocity. The moment coefficient increased with increasing velocity for negative angles of attack, and decreased for increasing velocity at positive angles of attack. The Glauert-Den Hartog stability criterion gives possible instabilities for all wind tunnel velocities tested. The possibly unstable angles of attack were from about -74 to -57°, at some angles close to zero, at some angles from 16 to 26°, and lastly for some angles from 55 to 64°. The Strouhal number was estimated to be 0.194.The galloping analysis provided many critical angles of attack coupled with critical velocities. Most of these angles were consistent with the Glauert-Den Hartog stability criterion, but one of the analyses found some that were not. The critical mode shapes showed many vertical modes for both small and large angles. Some of the large angles exhibited cross-wind movement at certain velocities. So, there's a possibility of galloping on this railway stretch, but all conditions must occur at the same time for this to happen. One limitation to the galloping analysis was the occurrence of vortex shedding in the wind tunnel. The calculations had a source of error when including the other elements of the catenary system. All the elements were assigned the same coefficients as the contact wire.

Acknowledgement

I would like to thank my main supervisor, Ole Andre Øiseth, for being a motivation and great teacher of the methods. Also, thanks to Anders Rønnquist for insights on the design of the wind tunnel model.

Thanks to Nils Arne Snekvik at Sintef Ocean for 3D-printing the model. Thank you, Gøran Loraas from the laboratory staff at the Department of Structural Engineering, for helping me with the assembly. The other staff in the laboratory were also very helpful. The wind tunnel testing hadn't happened if it wasn't for Bjørn S. Schjølberg who helped with running the rig in the wind tunnel. Thank you, Bjørn!

I would also like to thank Petter Røe Nåvik for always helping when I turned up unannounced, and for providing me with the FE-model.

Table of Contents

List of Tables

List of Figures

Chapter 1

Introduction

1.1 Background

With an increasing need for environmentally friendly and effective transportation, it's important to understand all aspects of railway transport. New railway stretches are being build, old ones are reconditioned to fit new solutions. High speed trains are incorporated to a larger extent. The contact wire is one of the most important components, providing electricity to the train or tram. This transfer of energy should not be interrupted. Many have studied the dynamic relationship between the contact wire and the receiver on the train. Aerodynamic studies are becoming more and more important for this relationship. Wind effects are worth studying because of the long spans and low damping characteristics of the catenary system. Wind loading can lead to aerodynamic instabilities that, in addition to disturbing the energy transfer, can lead to wear on the contact wire system. Normal wear and tear of the contact wire can also lead to a change in aerodynamic constants (Stickland and Scanlon (2001)).

Galloping instabilities have occurred in e.g. the UK where part of the catenary system was experiencing galloping at wind velocities as low as 17.9 m/s (Stickland et al. (2003)). Galloping is also linked to ice build up, where the aerodynamic characteristics are changed. This has happened in North America, China, France, Japan, and Korea among others (Heyun et al. (2012) and Xie et al. (2014)).

High speed trains are, as mentioned, being introduced in several variations with different speeds. In China, wind effects have been a limiting factor when it comes to further increasing these speeds (Song et al. (2018)). This demonstrates the increasing need for understanding aerodynamic effects when introducing new technologies.

The understanding of the aerodynamic characteristics of the contact wire cross-section starts with the static coefficients for drag, lift and pitching moment. Wind tunnel testing can determine the coefficients and other aerodynamic characteristics. The coefficients can be used to investigate galloping instabilities.

1.2 Objectives

The main objectives are

1. Determine static aerodynamic coefficients of an AC-120 contact wire
2. Express the results with a stability criterion
3. Determine Strouhal number for the contact wire
4. Perform a galloping analysis on a finite element model of a catenary system to determine if galloping can occur

1.3 Approach

The drag, lift and moment coefficients are determined by wind tunnel experiments for different angles of attack of the flow and for different wind velocities. The coefficients are also determined for different Reynolds numbers with angle of attack equal to zero. The stability criterion chosen to plot the results was the Glauert-Den Hartog criterion. The Strouhal number for the contact wire is also determined from wind tunnel results for an angle of attack of zero. The galloping analysis is performed on an Abaqus-model of a real catenary system using the determined aerodynamic coefficients.

1.4 Structure of the Master Thesis

The structure of the remaining chapters is as follows.

Chapter 2: Necessary theory including overview of a catenary system, theory on aerodynamic instabilities, buffeting theory, scaling laws, and random vibration theory

Chapter 3: Design of the wind tunnel model

Chapter 4: Methods for the wind tunnel experiment

Chapter 5: Description of the galloping analysis and its elements

Chapter 6: Results and discussion of the aerodynamic coefficients, the stability criterion, the Strouhal number calculations, and the galloping analysis

Chapter 7: Conclusion and suggestions for further work

Chapter 2

Theory

2.1 Overview of the Catenary system

The catenary system consists of the elements shown in figure 2.1. The components of the system are all part of the transfer of electrical energy to the electrical current collecter on the train, the pantograph. The contact wire transfers electricity to the train. The messenger wire's task is to support the contact wire. It distributes the tension forces in the wires with help from the droppers which connects the messenger wire to the contact wire . The support poles supports the wires with carrying poles. The carrying poles have registration arms connected to steady arms which holds the contact wire. The stitch wire is connected to the droppers and hangs below the messenger wire at support poles. The bracket supports the messenger wire.

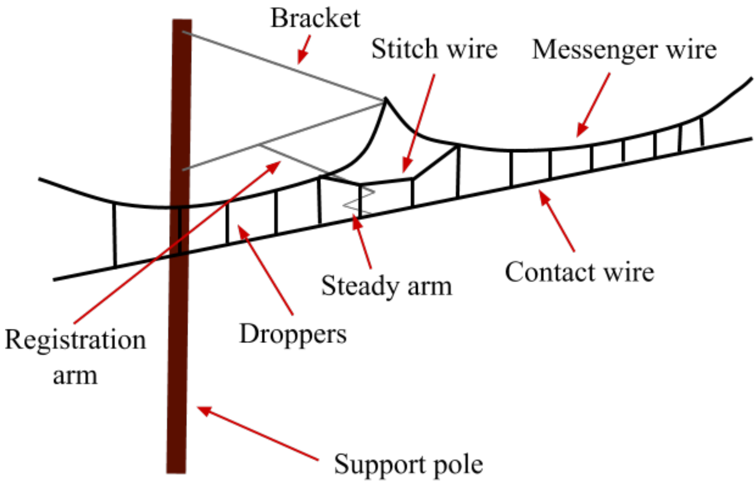

Figure 2.1: The catenary system

2.1.1 The Contact Wire

The transfer of energy through the contact wire needs to be steady and uninterrupted. The cross-section area and material is dependent on the speed of the train. The material is copper or a copper alloy. An example of a contact wire cross-section is shown in figure 2.2. The contact wire is exposed to wind. The grooves in the contact wire can lead to aerodynamic forces which in turn can lead to aerodynamic instabilities. These instabilities can interrupt the energy transfer.

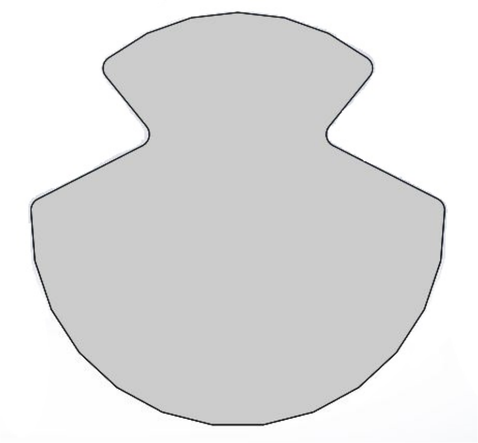

Figure 2.2: Example of contact wire cross section

2.2 Static Wind Forces

The static forces considered are shown in figure 2.3. The forces are considered in 2D as a simplification because the most interesting case is the response when the wind flow comes in perpendicular to the structures longitudinal axis. Drag force is a force induced on a body by a fluid in the direction of the flow . The drag force can be divided into a pressure and a shear (or friction) component. Pressure drag is because of difference in pressure upstream and downstream of the immersed body. Shear drag is caused by the viscosity of the fluid and the boundary layer profile of the flow around the body. Lift is a force induced on a body perpendicular to the flow. As for drag, both friction and pressure make contributions on the lift force. The aerodynamic moment considered in 2D is the pitching moment which is applied at the aerodynamic center of the cross-section. Equation (2.1) describe drag force, lift force and pitching moment.

$$F_D = \frac{1}{2}\rho U^2 C_D D L \tag{2.1a}$$

$$F_L = \frac{1}{2}\rho U^2 C_L B L \tag{2.1b}$$

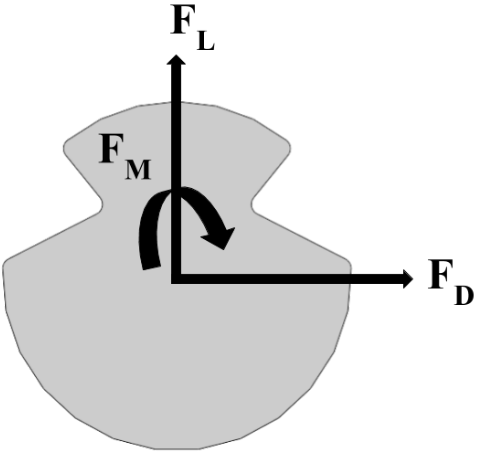

Figure 2.3: Static forces in 2D.

$$F_M = \frac{1}{2}\rho U^2 C_L B^2 L \tag{2.1c}$$

where ρ is the density of air, U is the wind velocity, D is the height of the cross section, B is the width of the cross section and L is the length of the body. The forces can be measured in a wind tunnel experiment to determine the drag, lift and pitching moment coefficients denoted C_D, C_L and C_M. The coefficients are dependent on the angle of attck, α (eq.(2.2)).

$$C_D(\alpha) = C_D(\overline{\alpha}) + \alpha_f C_D^{'}(\overline{\alpha}) = \overline{C}_D + \alpha_f C_D^{'} \tag{2.2a}$$

$$C_L(\alpha) = C_L(\overline{\alpha}) + \alpha_f C_L^{'}(\overline{\alpha}) = \overline{C}_L + \alpha_f C_L^{'} \tag{2.2b}$$

$$C_M(\alpha) = C_M(\overline{\alpha}) + \alpha_f C_M^{'}(\overline{\alpha}) = \overline{C}_M + \alpha_f C_M^{'} \tag{2.2c}$$

where $\overline{\alpha}$ is the mean value and α_f is the fluctuating part of the attack angle. $C_D^{'}$, $C_L^{'}$ and $C_M^{'}$ are the slopes of the coefficients at mean angle of attack. (Tamura and Kareem (2013))

2.3 Aerodynamic Instabilities

Aerodynamic effects can be arranged into two categories; wind induced and motion induced response. Wind induced response consist of buffeting and vortex induced response. Buffeting theory describes a structures response to the fluctuating component of the wind, which is divided into a static and fluctuating part. Buffeting theory is described in section 2.4. Vortex induced response is a result of flow separation at the surface of a body immersed in flow. Motion induced instabilities cause large changes in the structure response based on small variations in loading. Examples of this is static divergence, galloping and flutter. Galloping is the most relevant instability for a structure consisting of cables or wires.

2.3.1 Vortex Shedding

The vortices are created at the separation points of a body immersed in flow. Since the body has two separation points at the sides of the body, the vortices are created and released in an alternating and periodic manner. The change in pressure from the vortices give way to fluctuating forces exciting the body to oscillate. The oscillation is mainly from fluctuating lift forces, but there's also smaller fluctuating drag forces. Vortex shedding occurs in steady, laminar flow where the periodic behaviour isn't interrupted. The oscillation occurs when the shedding frequency, f$_s$ is equal to the natural frequency of the body, f$_n$. The shedding frequency is linked to wind velocity through the Strouhal number (eq. (2.3)).

$$S_t = \frac{f_s D}{V} \tag{2.3}$$

Equation (2.3) can be used to find the critical velocity for vortex shedding when f$_s$ = f$_n$. A phenomenon called lock-in occurs in an interval around the critical velocity. What happens is that the shedding frequency remains constant and equal to the natural frequency, i.e. equation (2.3) is not valid. The oscillation from vortex shedding is self-destructive since larger displacement at lock-in interrupts the cause. Vortex induced vibration is a small-amplitude oscillation. The response is nominal when the shedding frequency isn't equal to a natural frequency. The displacement is larger around natural frequencies, but still much smaller than the diameter of the cross-section.

2.3.2 Galloping

Galloping is a one dimensional instability in the cross-wind direction. In contrast to vortex shedding, galloping is a large-amplitude oscillation where the displacement ranges from one to more than ten times the diameter of the cross section. The oscillations are motion induced meaning that the motion causes a variation in angle of attack which in turn causes changes to the cross-wind forces. These changes are in phase with the motion yielding larger and larger oscillations. Galloping is closely related to the damping. Galloping occurs when the magnitude of the aerodynamic damping is larger than the mechanical damping (see section 2.4 and 2.3.2). Galloping can occur in laminar and turbulent flows.

The Glauert-Den Hartog Stability Criterion

The Glauert-Den Hartog criterion is derived from the one-dimensional equation of motion of a system subjected to wind (eq. (2.4)).

$$m(\ddot{y} + 2\xi\omega\dot{y} + \omega^2 y) = -\frac{1}{2}\rho V D\Big(\frac{dC_L}{d\alpha} + C_D\Big) doty \tag{2.4}$$

Where the right hand side is an expression for the aerodynamic damping. Moving this expression to the left hand side gives an expression for the total damping shown in equation 2.5.

$$c_{tot} = 2m\xi\omega + \frac{1}{2}\rho V D\Big(\frac{dC_L}{d\alpha} + C_D\Big) \tag{2.5}$$

The system is unstable if the total damping is negative. For this expression to be negative, the term in the aerodynamic damping shown in equation (2.6) must be fulfilled. This applies because the mechanical damping ratio, ξ, is positive. It's worth repeating that the mechanical damping must be smaller than the magnitude of the aerodynamic damping so that $c_{tot} < 0$, in addition to the criterion in equation (2.6). (Stickland and Scanlon (2001))

$$\frac{dC_L}{d\alpha} + C_D < 0 \tag{2.6}$$

Flutter

Flutter follows the same concept at galloping, where energy is added to the oscillation so that a system experiences larger and larger oscillations. But flutter is more complex than galloping because it involves displacement in two or more degrees of freedom. Flutter is usually a combination of vertical and torsional modes where the mode shapes and natural frequencies are similar.

2.4 Buffeting Theory

The equation of motion for a multi-degree of freedom system is shown in equation (2.7).

$$M\ddot{\boldsymbol{r}}(x,t) + C\ddot{\boldsymbol{r}}(x,t) + K\boldsymbol{r}(x,t) = \boldsymbol{F}(t) \tag{2.7}$$

Where M is the mass matrix, K is the stiffness matrix, C is the damping matrix, $\boldsymbol{r}(x,t)$ is the displacement vector, and $\boldsymbol{F}(t)$ is the external force vector. x is the position along the longitudinal axis of the structure. Modal analysis can be applied to the equation of motion by introducing the replacement of $\boldsymbol{r}(x,t)$ with the substitution in equation (2.8).

$$\boldsymbol{r}(x,t) = \begin{bmatrix} r_y \\ r_z \\ r_\theta \end{bmatrix} = \boldsymbol{\phi}(x) \cdot \boldsymbol{\eta}(t) \tag{2.8}$$

where $\boldsymbol{\phi}(x)$ is the mode shape matrix calculated in the still-air eigenvalue problem, and $\boldsymbol{\eta}(t)$ is a vector with generalized coordinates. This substitution leads to an alternative form of the equation of motion (eq.(2.9)).

$$\tilde{M}\ddot{\boldsymbol{\eta}}(t) + \tilde{C}\dot{\boldsymbol{\eta}}(t) + \tilde{K}\boldsymbol{\eta}(t) = \tilde{\boldsymbol{Q}}_{tot}(t) \tag{2.9a}$$

$$\tilde{M} = \int_L \boldsymbol{\phi}^{\boldsymbol{T}}(x) M \boldsymbol{\phi}(x) dx, \quad \tilde{C} = 2\tilde{M}\omega\xi, \quad \tilde{K} = \omega^2 \tilde{M} \tag{2.9b}$$

where ω and ξ are assumed known from the still-air eigenvalue problem. The matrices $\tilde{M}$, $\tilde{C}$ and $\tilde{K}$ are the uncoupled modal system matrices, which means that they are diagonal. $\tilde{\boldsymbol{Q}}_{tot}(t)$ is the modal load vector defined as (eq.(2.10))

$$\tilde{\boldsymbol{Q}}_{tot}(t) = \int_L \boldsymbol{\phi}^{\boldsymbol{T}}(x) \boldsymbol{q}_{tot}(t) dx \tag{2.10}$$

where $\boldsymbol{q}_{tot}(t)$ is the cross-sectional load vector which contains the drag, lift and moment loads (eq. (2.11)).

$$\boldsymbol{q}_{tot}(t) = [q_y \quad q_z \quad q_\theta]_{tot}^T \tag{2.11}$$

Figure 2.4 shows the necessary displacements, angles and velocities to fully define the cross-sectional load vector. The convention, when considering wind contributions to the load vector, is to decompose the wind speed into a mean and a fluctuating part (eq.(2.12)). The mean is time-invariant and the fluctuating wind velocity is considered as a zero-mean variable.

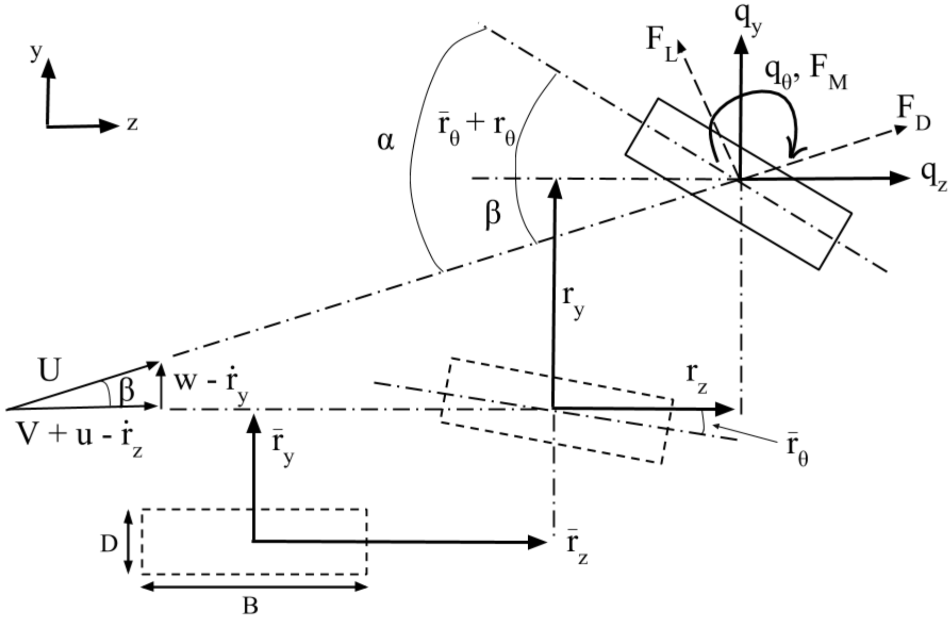

Figure 2.4: Cross-section of body immersed in flow with velocities and displacements. The static forces in equation (2.1) are also included.

$$V_{tot}(x,t) = \overline{V}(x) + \boldsymbol{v}(x,t) = V + \begin{bmatrix} u \\ w \end{bmatrix} \tag{2.12}$$

In figure 2.4, V is the mean speed of the wind field. And u and w are components of the fluctuating velocity, $\boldsymbol{v}(x,t)$. The mean wind causes an initial displacement, $\overline{\boldsymbol{r}}$. The fluctuations occur about this initial displacement and is denoted $\boldsymbol{r}$. The fluctuating displacement have derivatives $\dot{\boldsymbol{r}}$ and $\ddot{\boldsymbol{r}}$. α is the attack angle of the flow to the horizontal axis of the cross section. β is the dynamic wind angle which is caused by the fluctuations.

As a result of the wind decomposition, the cross-sectional load vector is decomposed into a flow induced and a motion induced component (eq. (2.13)).

$$\boldsymbol{q}_{tot}(t) = \overline{\boldsymbol{q}}(x,t) + \boldsymbol{q}_{ae}(x,t,\ddot{\boldsymbol{r}},\dot{\boldsymbol{r}},\boldsymbol{r}) = \begin{bmatrix} \overline{q}_y(x) \\ \overline{q}_z(x) \\ \overline{q}_\theta(x) \end{bmatrix} + \begin{bmatrix} q_y(x,t) \\ q_z(x,t) \\ q_\theta(x,t) \end{bmatrix} \tag{2.13}$$

Assuming small angles and neglecting higher order terms. The cross-sectional load vector takes the form (eq. (2.14))

$$\boldsymbol{q}_{tot}(x,t) = \overline{\boldsymbol{q}}(x,t) + B_q(x) \cdot \boldsymbol{v}(x,t) + C_{ae}(x) \cdot \dot{\boldsymbol{r}}(x,t) + K_{ae}(x)\boldsymbol{r}(x,t) \tag{2.14}$$

The different components of the cross-sectional load vector are defined in equation (2.15).

$$\overline{\boldsymbol{q}} = \frac{\rho V^2 B}{2} \begin{bmatrix} (D/B)\overline{C}_D \\ \overline{C}_L \\ B\overline{C}_M \end{bmatrix} \tag{2.15a}$$

$$B_q = \frac{\rho V B}{2} \begin{bmatrix} 2(D/B)\overline{C}_D & ((D/B)C_D^{'} - \overline{C}_L) \\ 2\overline{C}_L & (C_L^{'} + (D/B)\overline{C}_D) \\ 2B\overline{C}_M & BC_M^{'} \end{bmatrix} \tag{2.15b}$$

$$C_{ae} = -\frac{\rho V B}{2} \begin{bmatrix} 2(D/B)\overline{C}_D & ((D/B)C_D^{'} - \overline{C}_L) & 0 \\ 2\overline{C}_L & (C_L^{'} + (D/B)\overline{C}_D) & 0 \\ 2B\overline{C}_M & BC_M^{'} & 0 \end{bmatrix} \tag{2.15c}$$

$$K_{ae} = \frac{\rho V^2 B}{2} \begin{bmatrix} 0 & 0 & (D/B)C_D^{'} \\ 0 & 0 & C_L^{'} \\ 0 & 0 & BC_M^{'} \end{bmatrix} \tag{2.15d}$$

The modal load vector is now expressed as shown in equation (2.16).

$$\tilde{\boldsymbol{Q}}_{tot}(t) = \int\limits_L \Big(\boldsymbol{\phi}^{\boldsymbol{T}} \overline{\boldsymbol{q}} + \boldsymbol{\phi}^{\boldsymbol{T}} B_q \cdot \boldsymbol{v} + \boldsymbol{\phi}^{\boldsymbol{T}} C_{ae} \boldsymbol{\phi} \cdot \dot{\boldsymbol{\eta}}(t) + \boldsymbol{\phi}^{\boldsymbol{T}} K_{ae} \boldsymbol{\phi} \cdot \boldsymbol{\eta}(t) \Big) dx \tag{2.16}$$

$\boldsymbol{C}_{ae}$ and $\boldsymbol{K}_{ae}$ are the aerodynamic damping and stiffness matrices. They are linked to the displacement vector, $\boldsymbol{r} = \boldsymbol{\phi} \cdot \boldsymbol{\eta}$. This leads to a rearrangement of the generalized equation of motion (eq. (2.9a)). The rearrangement is shown in equation (2.17).

$$\tilde{M}\ddot{\boldsymbol{\eta}} + (\tilde{C} - \tilde{C}_{ae})\dot{\boldsymbol{\eta}} + (\tilde{K} - \tilde{K}_{ae})\boldsymbol{\eta} = \int\limits_L \Big(\boldsymbol{\phi}^{\boldsymbol{T}} \overline{\boldsymbol{q}} + \boldsymbol{\phi}^{\boldsymbol{T}} B_q \cdot \boldsymbol{v} \Big) dx = \tilde{\boldsymbol{Q}}(t) \tag{2.17}$$

Where $\tilde{C}_{ae}$ and $\tilde{K}_{ae}$ are the generalized aerodynamic damping and stiffness matrices. The buffeting theory is taken from Strømmen (2010).

2.4.1 Polynomial Eigenvalue Problem

The new equation of motion with zero load vector, $\tilde{\boldsymbol{Q}}(t)$, can be expressed as the polynomial eigenvalue problem (eq.(2.18)). The eigenvalue problem is no longer linear because it includes damping. Dowell (2014).

$$s^2 \cdot \tilde{M} + s \cdot (\tilde{C} - \tilde{C}_{ae}) + (\tilde{K} - \tilde{K}_{ae}) = 0 \tag{2.18}$$

The solution to the this eigenvalue problem is of the form shown in equation (2.19), where s is the eigenvalue. The eigenvalue is complex and its components are represented in equation (2.20). ξ is the damping ratio, ω_n is the natural frequency of an undamped system and ω_d is the damped frequency.

$$y(t) = e^{st} \qquad s = a \pm ib \tag{2.19}$$

$$a = real(s) = -\xi \cdot \omega_n \qquad b = imag(s)\omega_d = \omega_n \cdot \sqrt{1-\xi^2} \tag{2.20}$$

The polynomial eigenvalue problem will result in complex mode shapes as well. Here the displacement is dependent on both amplitude and phase angle, unlike real (normal) modes. The complexity is physical, but can also be partly numerical. The physical part is a result of non-proportional damping, aerodynamic effects, and other non-linearities. Numerical complexity can be a result of errors in the process of estimating the frequencies and mode shapes. One method of plotting complex mode shapes with real values is shown in equation (2.21).

$$\boldsymbol{\phi} = \boldsymbol{X} \cdot e^{st} \tag{2.21}$$

Where $\boldsymbol{X}$ is the complex mode shape, t is a time vector which is necessary because of the complexity of $\boldsymbol{X}$ and s.

2.5 Scaling Laws

2.5.1 Reynolds Number

When performing wind tunnel tests it's important that the Reynolds number is kept constant. So an upscaling of the cross-section which leads to a increased deterministic length must lead to a corresponding reduction in the wind velocity to keep the Reynolds number in equation (2.22) constant.

$$Re = \frac{\rho V D}{\mu} \tag{2.22}$$

ρ is the density of air(fluid body is immersed in), V is the wind velocity (velocity of fluid around body), D is the characteristic length of the body (in this case the diameter of the contact wire (diameter is the height), and μ is the dynamic viscosity of air (fluid).

2.5.2 Strouhal Number

The Strouhal number can be determined with wind tunnel testing on a scaled cross-section. The Strouhal number found in a wind tunnel experiment is equal to that of the normal scale geometry. Vortex shedding occurs in laminar flow, which is easy to accomplish in a wind tunnel. The experimental flow velocity must be close to where vortex shedding is most likely.

2.6 Random Vibration Theory

Analysis of random vibration is often performed in the frequency domain. The concepts of Fourier transformation and spectral densities are useful tools for analyzing the frequency content of measurement data.

2.6.1 Fourier Series and Fourier Transform

A Fourier Series can describe any periodic behaviour by a series of sine and cosine terms multiplied with a constant.

$$x(t) = a_0 + \sum_{k=1}^{\infty} \left(a_k cos \frac{2\pi k}{T} t + b_k sin \frac{2\pi k}{T} t \right) = a_0 + \sum_{k=1}^{\infty} \left(a_k cos \omega_k t + b_k sin \omega_k t \right) \tag{2.23}$$

where a_0, a_k, b_k are the constants also known as the Fourier coefficients. And $\omega_k = \frac{2\pi k}{T}$. The Fourier series becomes a Fourier integral if the period $T \rightarrow \infty$.

$$x(t) = \int_{0}^{\infty} 2 \left(A(\omega) cos \omega t + B(\omega) sin \omega t \right) d\omega \tag{2.24}$$

where

$$A(\omega) = \frac{1}{2\pi} \int_{-\infty}^{\infty} x(t) cos \omega t dt \qquad \wedge \qquad B(\omega) = \frac{1}{2\pi} \int_{-\infty}^{\infty} x(t) sin \omega t dt \tag{2.25}$$

are the components of the Fourier transform. Equation (2.24) is the inverse Fourier transform. In random vibrations it's necessary to define a complex version of the Fourier transform (eq. (2.26)).

$$X(\omega) = A(\omega) - iB(\omega) = \frac{1}{2\pi} \int_{-\infty}^{\infty} x(t) e^{-i\omega t} dt \tag{2.26}$$

For a sampled signal, x_r the Fourier transform becomes discrete, DFT (eq.(2.27)).

$$X_r = \frac{1}{N} \sum_{r=0}^{N-1} x_r e^{-i(2\pi k r / N)} \qquad k = 0, 1, 2, ..., (N-1) \tag{2.27}$$

Where x_r consists of N sample values. (Newland (2005))

2.6.2 Correlation

Two variables are said to be correlated to some degree if the change of one leads to a distinct change in the other. The correlation coefficient is defined in equation (2.28).

$$\rho_{xy} = \frac{E\left[(x - E[x])(y - E[y]) \right]}{\sigma_x \sigma_y} \tag{2.28}$$

It represents the existence of a straight regression line in a plot of x and y values. ρ can take values from +1 to -1. If $\rho_{xy} = \pm 1$ there is a perfect correlation between x and y, if $\rho_{xy} = 0$ there's no correlation between the variables.

2.6.3 Auto-Correlation Function

The auto-correlation function, R_x, describes the correlation of a time series, x(t), with itself after a time lag, τ.

$$R_x(\tau) = E\left[x(t)x(t+\tau)\right] \tag{2.29}$$

The auto-correlation is only dependent on τ because the process is stationary. The function is even in τ.

2.6.4 Cross-Correlation Function

The cross-correlation function describes the correlation of a time series x(t) with another time series y(t+τ).

$$\begin{aligned} R_{xy}(\tau) &= E\left[x(t)y(t+\tau)\right] \\ R_{yx}(\tau) &= E\left[y(t)x(t+\tau)\right] \end{aligned} \tag{2.30}$$

The cross-correlation function is also only dependent on τ given that the two processes are stationary, but not even in τ. Note that $R_{xy} \neq R_{yx}$ (Newland (2005)).

2.6.5 Spectral Densities

Auto Spectral Density

The auto spectral density of a time series, x(t), is defined as the Fourier transform of the auto-correlation function of x (eq. (2.31)).

$$S_x(\omega) = \frac{1}{2\pi} \int\limits_{-\infty}^{\infty} R_x(\tau) e^{-i\omega\tau} d\tau \tag{2.31}$$

The Fourier transform can only be evaluated if the process x(t) has a mean value of zero, or else the integral in equation (2.31) will be equal to ∞. So, to inspect the frequency content of a stochastic process one should standardize x(t), given that the process is without periodic components (Newland (2005)).

Cross Spectral Density

The cross spectral density is defined as the Fourier transform of the cross-correlation function of two stochastic processes, x(t) and y(t) (eq.(2.32)).

$$S_{xy}(\omega) = \frac{1}{2\pi} \int\limits_{-\infty}^{\infty} R_{xy}(\tau) e^{-i\omega\tau} d\tau \tag{2.32}$$

Here, it's also important to remember that $S_{xy} \neq S_{yx}$, but we do have the relation in equation (2.33). Where * denotes the complex conjugate.

$$S_{yx}(\omega) = S^*_{xy}(\omega) \tag{2.33}$$

The spectral densities are density functions, which means that the areas below the functions are important.

$$Area = \int_{-\infty}^{\infty} S_x(\omega)d\omega = R_x(\tau = 0) = E\left[x(t)x(t)\right] = \sigma^2 \tag{2.34}$$

Note that equation (2.34) is valid for a process with zero mean. This equation shows a relation between the spectral density and the standard deviation of x. Therefore, looking at the frequency content of a sample through the spectral densities can give important statistical information on the process x(t) at different frequencies.

The Fast Fourier transform (FFT) is a more efficient way of determining the spectral density of a time series compared to calculating the DFT of the correlation. The method finds the spectral density straight from the time series itself, without determining the correlation first (Newland (2005)). The auto spectral density of a signal, x(t), would be as expressed in equation (2.35)

$$S_{xx}(\omega) = \frac{X(\omega) \cdot X^*(\omega)}{\Delta\omega} \tag{2.35}$$

where X(ω) is the FFT of x(t), X$^*(\omega)$ is the complex conjugate, and $\Delta\omega = \frac{2\pi}{T}$ where T is the length of the time series.

2.6.6 Sampling frequency

A measurement is a discrete quantity of points sampled with a time spacing in between. The time spacing is crucial to representing the signal sufficiently. And the position and number of measuring points, as well as choice of hardware is important to guarantee a successful representation of the system and its characteristics. The sampling frequency should be equal to or higher than the Nyquist sampling rate, which is defined as twice the maximum frequency in the signal, $f_{Nyquist} = 2f_{max}$. The sampling frequency is found from the time spacing as $f_s = \frac{1}{\Delta t}$. If the sampling frequency is lower than the Nyquist frequency, aliasing occurs. Unnecessary information is stored if the sampling frequency is higher than the Nyquist frequency (Newland (2005)).

Chapter 3

Wind Tunnel Model

A few different properties were considered in making of the wind tunnel model. Two different cross-section were considered; up-scaling of 5 and 10 were compared. Firstly, the scaling of the cross-section is important for obtaining good measurements. Good measurements would be large enough to be properly picked up by the loading cells. So this means that the cross-section had to be large enough to present sufficient resistance to the flow in the wind tunnel. Previous contact wire wind tunnel studies have used e.g. the scale 2:1 (Xie et al. (2014)) and scale 10:1 (Stickland and Scanlon (2001)).

Since the plan was to make the contact wire cross-section in a plastic foam material one has to add stiffness to the model. This is done by adding an aluminum pipe. The contact wire shape is hollow below the grooves to fit the pipe. Also, the loading cells are designed to hold a circular cross section with a diameter of 40 mm. So the pipe doubles as a connection between the contact wire shape and the mountings in the wind tunnel. Two aluminum pipes with thickness 1 mm and 3 mm were compared.

After the design was chosen, the production of the contact wire part was altered. It was supposed to be a Gurit® PVC material, but the dimensions around the aluminum pipe were so small that it was proposed to 3D-print the contact wire cross-section instead. A 3D-printed part would mean that the model would be much heavier than anticipated.

3.1 Alternatives to Model Design

3.1.1 Material and Section Properties

The materials considered for the model were initially Gurit® PVC 60 and aluminum. The material constants used in calculations for model design are shown in table 3.1. The pipe is part of the final model, and it also works as the connection between the cross-section shape and the loading cells. A 40 mm aluminum pipe fits into the mounting part on the loading cells in the wind tunnel. The calculations made uses the stiffness of the aluminum pipe as the total stiffness (eq. (3.4)-(3.3)).

Table 3.1: Material properties. [1]: Gay and Gambelin (2008), [2]: Gurit (n.d.).

	Aluminum [1]	Gurit® PVC 60 [2]
E_t [MPa]	70e3	100
ρ [kg/m^3]	2800	60

Table 3.2: Section properties

	CW shape with 40 mm hole		Aluminum pipe	
	Scale 5:1	Scale 10:1	t = 1 mm	t = 3 mm
D [m]	0.06562	0.1313	40e-3	40e-3
A [m^2]	1.73466e-3	0.01070855	1.2252e-4	3.487e-4
I_y [m^4]	6.1471293e-7	1.302283066e-5	2.330983e-8	6.00665e-8
I_z [m^4]	5.577679e-7	1.080924204e-5	2.330983e-8	6.00665e-8

3.1.2 Stability Calculations

A few properties were calculated and compared when designing the model. First the natural frequency was estimated from the equation (3.1) for a simply supported beam.

$$f_n = \frac{\pi}{2}\sqrt{\frac{EI}{mL^4}} \tag{3.1}$$

The total mass of the model is calculated in table 3.3 by using equation (3.2) and cross-section properties given in table 3.2. And the stiffness EI is provided by the aluminum pipe as indicated in equation (3.3) and (3.4).

$$m_{tot} = m_{ALU} + m_{GURIT} \tag{3.2}$$

$$E = E_{ALU} \tag{3.3}$$

$$I = I_{ALU} \tag{3.4}$$

Table 3.3: Calculation of total mass

		Aluminum pipe t = 1 mm		Aluminum pipe t = 3 mm	
[kg/m]	Original CW	Scale 5:1	Scale 10:1	Scale 5:1	Scale 10:1
m_{ALU}	-	0.343	0.343	0.97636	0.97636
m_{GURIT}	-	0.1040796	0.642513	0.1040796	0.642513
m_{tot}	1.08	0.4470796	0.985513	1.0804396	1.618873

The critical wind velocity for vortex shedding was calculated with equation (3.5) based on the Strouhal number of a cylinder, S_t = 0.2 and setting the vortex shedding frequency, f_s, equal to the natural frequency.

$$V_{CR} = f_s \cdot \frac{D}{S_t} \tag{3.5}$$

The Scruton number was calculated to determine aerodynamic stability during testing. The Scruton number represents mass-damping effects in the structure. And can indicate the risk of lock-in effects. A low Scruton number indicates that the model is more easily excited and susceptible to lock-in (Flamand (1995)). The Scruton number is also linked to across-wind vibration amplitude; an increase in Scruton number will decrease the amplitude (Ammann et al. (2011)). So a larger Scruton number is wanted. The Scruton number is calculated from equation 3.6.

$$S_c = \frac{2\delta_s m_e}{\rho b_{ref}^2} \tag{3.6}$$

where ρ is the density of air (here: 1.225 kg/m^3), b_{ref} is the characteristic width which is the diameter, m_e is the mass per unit length, and δ is the logarithmic decrement of the structural damping.

Table 3.4: Stability calculations for different scale-pipe combinations.

	Aluminum pipe t = 1 mm		Aluminum pipe t = 3 mm	
	Scale 5:1	Scale 10:1	Scale 5:1	Scale 10:1
m_{tot} [kg/m]	0.447	0.986	1.08	1.62
f_n [Hz]	12.73	8.58	13.15	10.74
V_{CR} [m/s]	4.18	5.63	4.3	7.05
S_c (ξ = 0.5 %)	5.3	2.9	12.9	4.8
S_c (ξ = 1 %)	11	5.9	25.7	9.6
S_c (ξ = 5 %)	53	29	128.6	48.14

3.1.3 Estimate of Force Measurements

Estimates of measured drag force (eq.(2.1a)) was also calculated to ensure sufficiently large measurements, with drag coefficient, $C_D = 1$. The calculations are shown in table 3.5. One can see that it's necessary to test for wind velocities of at least 3 m/s and 4 m/s to get measurements larger than 1 N. The scale 10:1 is limited to testing velocities above 3 m/s.

Table 3.5: Estimate of drag force measurements, F_D [N].

V [m/s]	Scale 5:1	Scale 10:1
1	0.11	0.22
2	0.43	0.88
3	0.98	2.0
4	1.7	3.5
5	2.7	5.5
6	3.9	7.9
7	5.3	11
8	7.0	14
9	8.9	18
10	11	22
11	13	27

3.1.4 Conclusion from Stability Calculations

Based on the stability calculations presented in table 3.4, the scale-pipe combination chosen was a scale of 5:1 with aluminum pipe with 3 mm thickness. The critical velocity is lower than for the scale 10:1, which might give smaller amplitude vibration during vortex shedding. The critical velocity is also smaller than 6 m/s which will be one of the wind tunnel velocities tested (6 m/s is analogous to 30 m/s on a real life contact wire using scale 5:1). The lowest critical velocity is for the scale 5:1 with 1 mm aluminum pipe, but this option has lower Scruton numbers, so a possible instability might be worse. There's also an issue with the scaling 10:1 considering the Reynolds number equivalence. The 'normal' wind velocities in Norway are up to 30 m/s. For scale 10:1 this equals 3 m/s in the wind tunnel, which is very low. It's also of interest to test a lower velocity. This means that the scaling 10:1 will probably not provide satisfactory measurements. A test with such a low wind velocity will probably not generate large enough forces in the loading cells. So the low velocity testing cancels out the effect of a larger cross-section when in comes down to measuring drag forces. The larger scaling option is discarded. And the scale 5:1 seems to give large enough drag force measurements. The final cross-section shape of the contact wire part of the model is shown in figure 3.1. The model is based on the shape of an AC-120 contact wire, and the scale is 5:1.

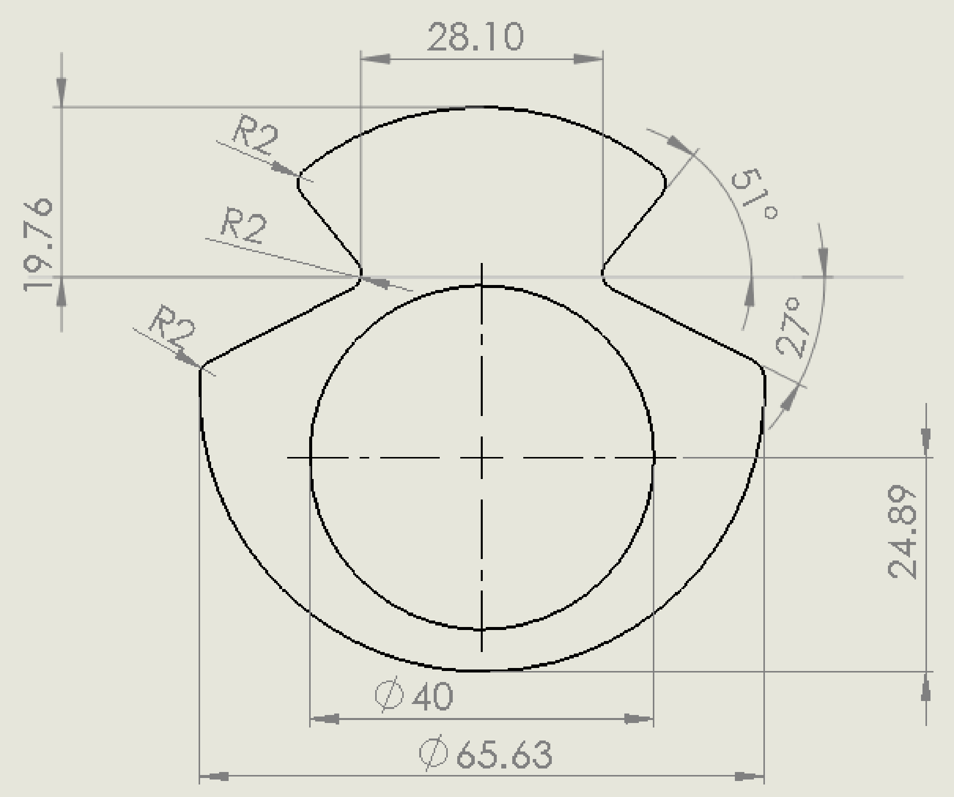

Figure 3.1: Final design of contact wire part of wind tunnel model. The outer shape is equal to an AC-120 contact wire, scaled 5:1. [mm]

3.2 Material Change

Some complications arose after choosing the final design. The original idea was to make the contact wire cross-section with a Gurit® PVC 60 material. This scaling with a 40 mm hole in the middle turned out to be a challenging shape. The model was to be milled and the process is demanding with such thin walls. The thinnest part is the distance from the innermost part of the grooves to the hole made to hold the aluminum pipe. The weight of the model wasn't an issue since the scope was to measure static forces. It was therefore decided to 3D-print the contact wire shape. A 3D-print gives a heavier model rendering some of the calculations in section 3.1.2 useless. A heavier model gives an even larger Scruton number, which is a positive trait. The stiffness of the plastic in the 3D-print was not known, so new calculations for critical velocity for vortex shedding was not made. But the stiffness is larger than for the Gurit® material. The stiffness can be determined in a natural frequency test. And possible vortex shedding instabilities can be controlled by people holding the model.

3.3 Building the Model

The contact wire part of the model was printed by Nils Arne Snekvik at Sintef Ocean AS in Trondheim. The print consisted of 12 parts; half-shells to be assembled around the aluminum pipe. The cross-section shape of the half-shells is shown in figure 3.2. Ten of the half-shells were of the same length, the other two were shorter. The parts used in the final section model are presented in table 3.6.

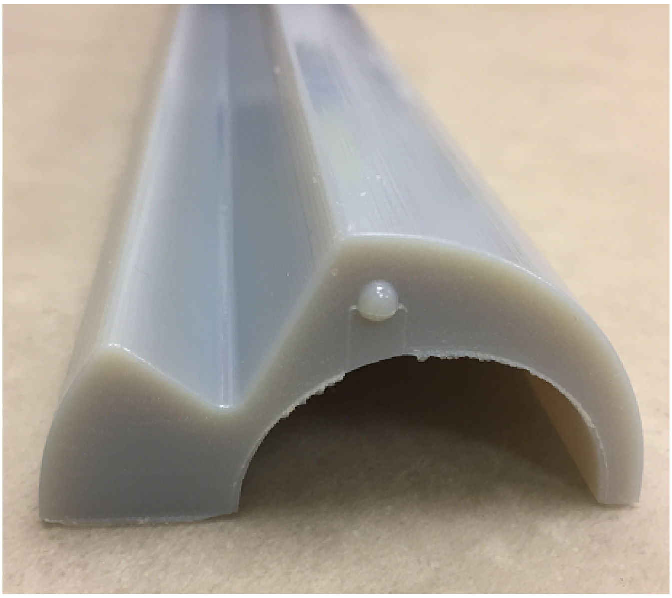

Figure 3.2: Cross-section shape of 3D-printed half-shells.

Table 3.6: Model parts

Part	Purpose	Dimension
Aluminum pipe	Stiffness contributor Correct dimensions for mounting in the wind tunnel	40x3 mm, length 2730 mm
3D-printed plastic parts	Contact wire shape Stiffness contributor	10 pcs. length 490 mm 2 pcs. length 230 mm
Araldite Standard Ultra	Adherent and crack filler	
Spray paint	Surface treatment	

The assembly of the model was done in the laboratory at the Department of Structural Engineering with help from Gøran Loraas. First the 3D-printed parts were filed to remove rough edges. This was necessary as one can see in figure 3.2. The plastic parts and the aluminum pipe were cleaned. The 3D-printed plastic parts were glued around the aluminum pipe. The half-shells have notches and fillings to ensure proper joining of all the pieces. One of the fillings can be seen in figure 3.2. The half-shells were glued together at the ends and to the aluminum pipe as shown in figure 3.3. The aluminum pipe is longer than the 3D-printed parts so there's 2.5 cm of uncovered aluminum pipe on each side. The parts were held together with clamps, and taped together to ensure a tight fit since the glue expands. The glue takes about 8 hours to dry, so the model was left as shown in figure 3.4.

There were cracks in the model after the glue had dried, so it was necessary to fill these. The same glue used doubled as a crack filler. Before and after crack filling is shown in figure 3.5. Excess glue was removed with a file after drying. The glue and the 3D-print have very different surface properties. The model was coated with spray paint to make the surface roughness constant, and to mask the stickiness of the glue. The model can't be disassembled.

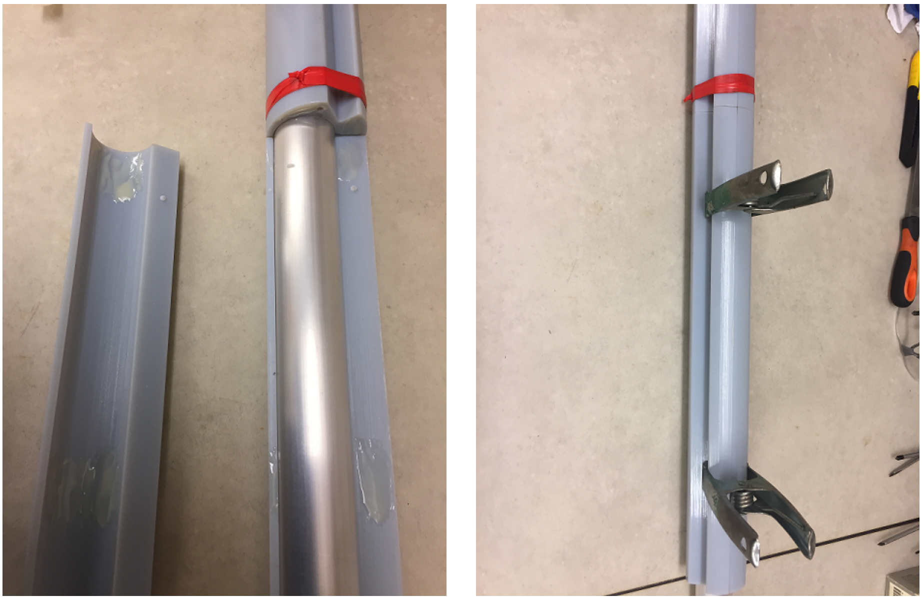

Figure 3.3: Gluing of 3D-printed parts to aluminum pipe.

3.4 Model Characteristics

The model has the lengths shown in figure 3.6. The aluminum pipe is 2.73 meters long, and the plastic contact wire is 2.68 meters long. The total weight is 7.951 kg. Where the pipe makes up 2.665 kg and the plastic contact wire shape makes up 5.286 kg. Mass per length is 2.912 kg/m.

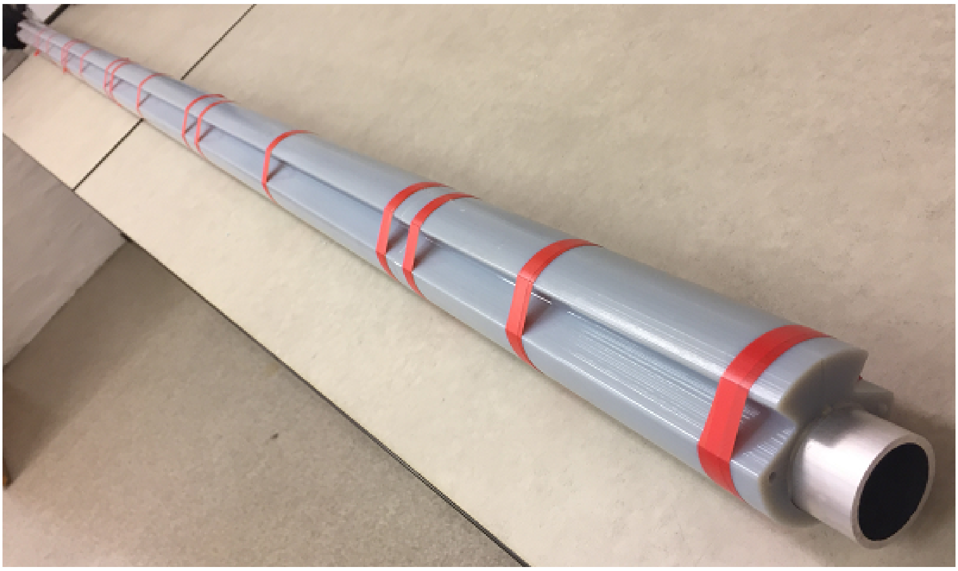

Figure 3.4: Tape holds the parts together while the glue dries.

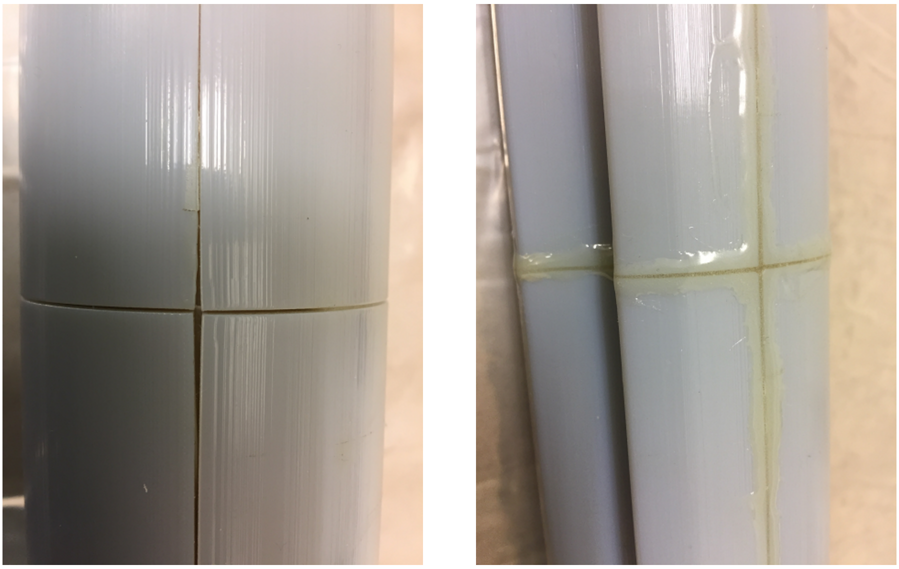

Figure 3.5: Filling cracks with glue.

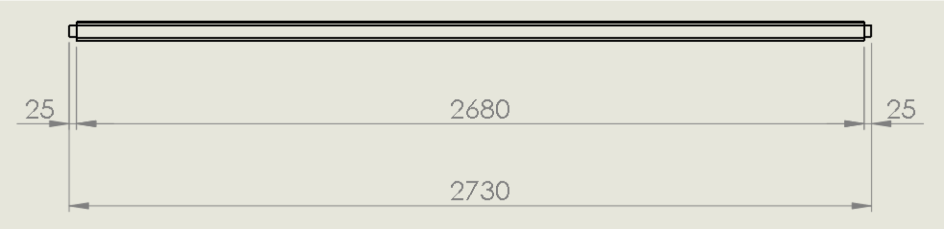

Figure 3.6: Drawing of lengths, [mm]. Assembly seen from above.

Chapter 4

Wind Tunnel Experiment

The wind tunnel testing was performed in the Fluid Mechanics Laboratory at the Department of Energy and Process Engineering, NTNU Gløshaugen. The purpose of the wind tunnel testing was to obtain aerodynamic coefficients which could be used to complete aerodynamic instability analyses. Figure 4.1 shows the model during a random testing sequence. The rotation simulates a positive angle of attack. The flow comes from the left. The model was tested at three wind velocities at angles of attack ranging between -75 to 75°. A natural frequency test was also performed.

Figure 4.1: Random testing sequence.

4.1 Equipment

The equipment used in the experiment is a Pitot probe, digital thermometer, the wind tunnel, and a rig with loading cells constructed by the Department of Structural Engineering at NTNU. The model is mounted on the loading cells and is fixed at both ends. The rig can be programmed to move, in this case to rotate the model about its longitudinal axis. One of the loading cells has a master rotor while the other has a slave rotor (fig. 4.2). The rig measures voltage in the two loading cells placed on opposite sides of the wind tunnel width. The loading cells can measure forces in the horizontal, lateral, and vertical direction as well as moments about all three axes, so there is in total six force measurements in each loading cell. The software of the rig can move the model in the vertical and lateral directions as well as rotation about the horizontal (longitudinal) axis. The anemometer (fig. 4.3) is placed behind the model in figure 4.2 so that it measures the wind speed before the flow reaches the model.

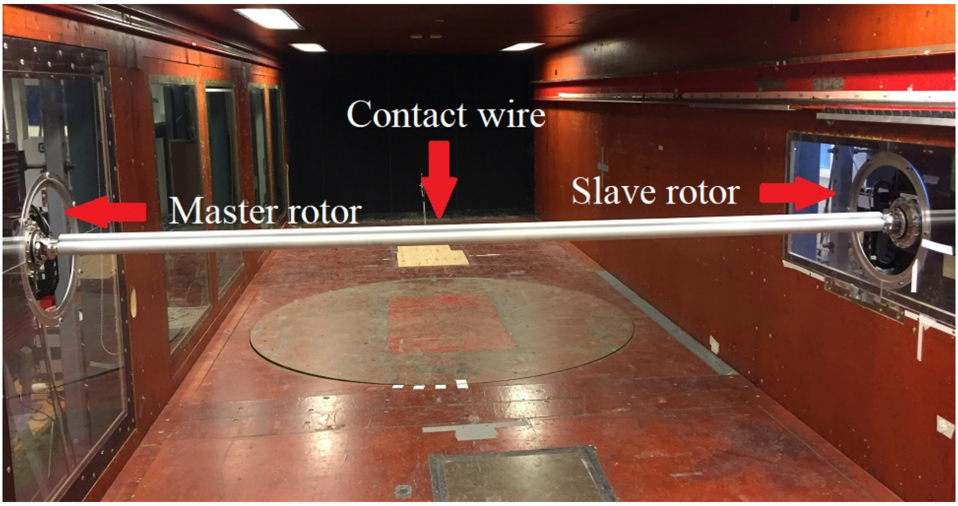

Figure 4.2: CW-model mounted on the loading cells in the wind tunnel

Figure 4.3: Pitot probe mounting

It's important to assemble the parts correctly when mounting the model in the loading cells. The parts are marked with "+X" and "+Y" to ensure axis alignment (fig. 4.4). The marks for positive y-direction were pointed upwards on both loading cells. The marks for positive x-direction were pointing in different directions since the loading cells are facing each other. This means that the lateral measurements from the loading cells should be of equal magnitude, but with different sign.

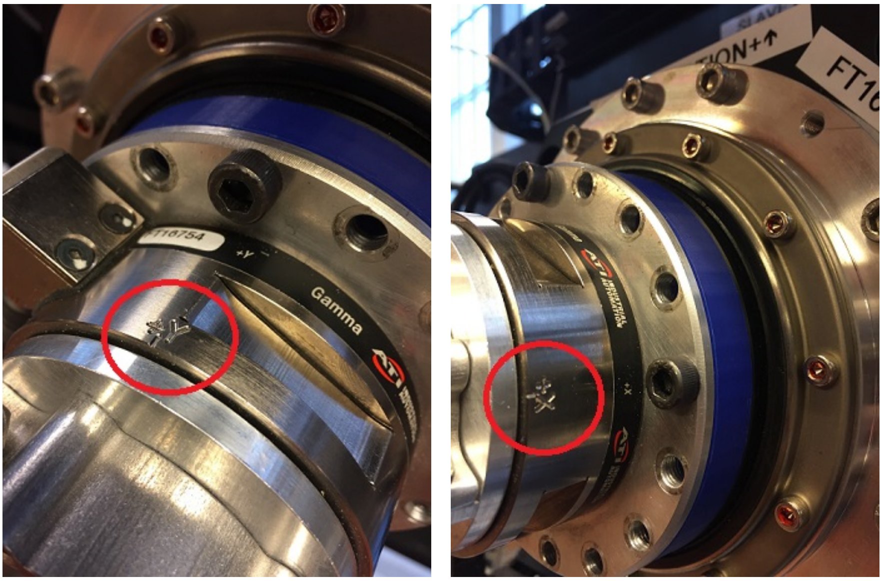

(a) Positive y-direction **(b)** Positive x-direction

Figure 4.4: Indications on parts to ensure alignment with the vertical and lateral axes.

The software used is LabVIEW. It logs forces as voltage measurements and wind velocity measurements from the anemometer on an USB flash drive. The user input is temperature and calibration coefficient for the anemometer. The software calculates air density and can plot the measurements in Volts or Newton. The user interface is shown in figure 4.6. The buttons circled with red are "Zero Bias" and "Start Logging". It's important to zero out bias before the data is logged. The section called "Log File Setup" is where the user defines how the data are stored on the flash drive. The section called "Wind Velocity" is where the user types in temperature and calibration coefficient. This section is magnified in figure 4.5.

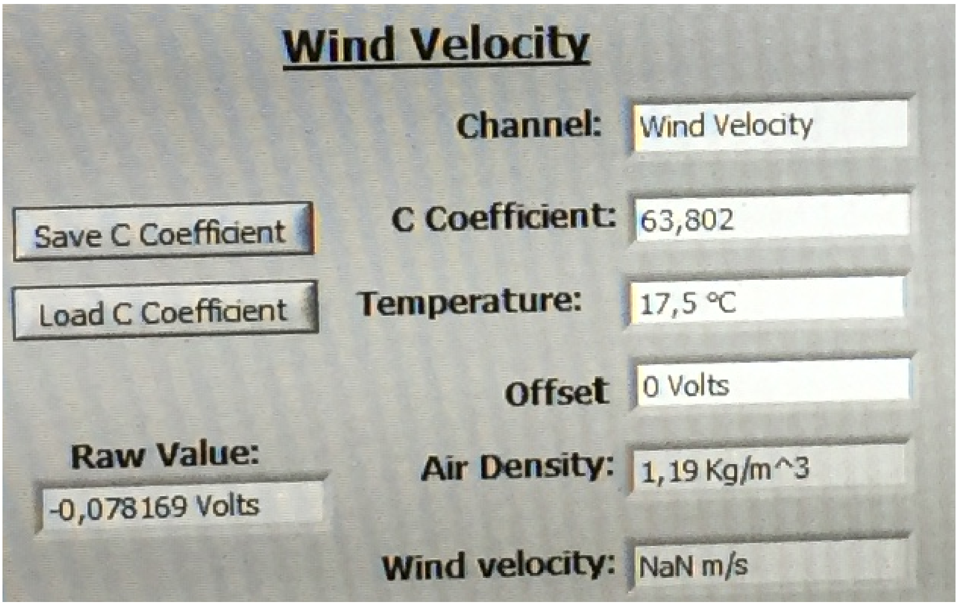

Channel: Wind Velocity
C Coefficient: 63,802
Temperature: 17,5 °C
Offset 0 Volts
Raw Value: -0,078169 Volts
Air Density: 1,19 Kg/m^3
Wind velocity: NaN m/s

Figure 4.5: Section of user interface for input of temperature and calibration coefficient.

4.2 Test Description

The anemometer and the software for the rig were calibrated. And the rotations for different attack angles were run before mounting the model into the loading cells, in case of errors. The model can break if there's an error in these scripts.

Three different wind velocities were tested; 4 m/s, 6 m/s and 10 m/s. Three different scripts were run on the software for each wind velocity. The scripts had intervals with different angles of attack to be tested. The scripts performed a rotation of the loading cells about the horizontal axis. Both loading cells had to be rotated in the same direction to avoid twisting the model. The scripts covered all integer angles from -75° to 75°. The model was kept at all integer angles for about six seconds. The first script had angles ranging from -75° to -25°. The second script had angles from -25° to 25°. And the third script tested angles from 25° to 75°. Figure 4.7 shows a selection of the model rotations. The wind flow in the tunnel comes in from the left-hand side towards the right.

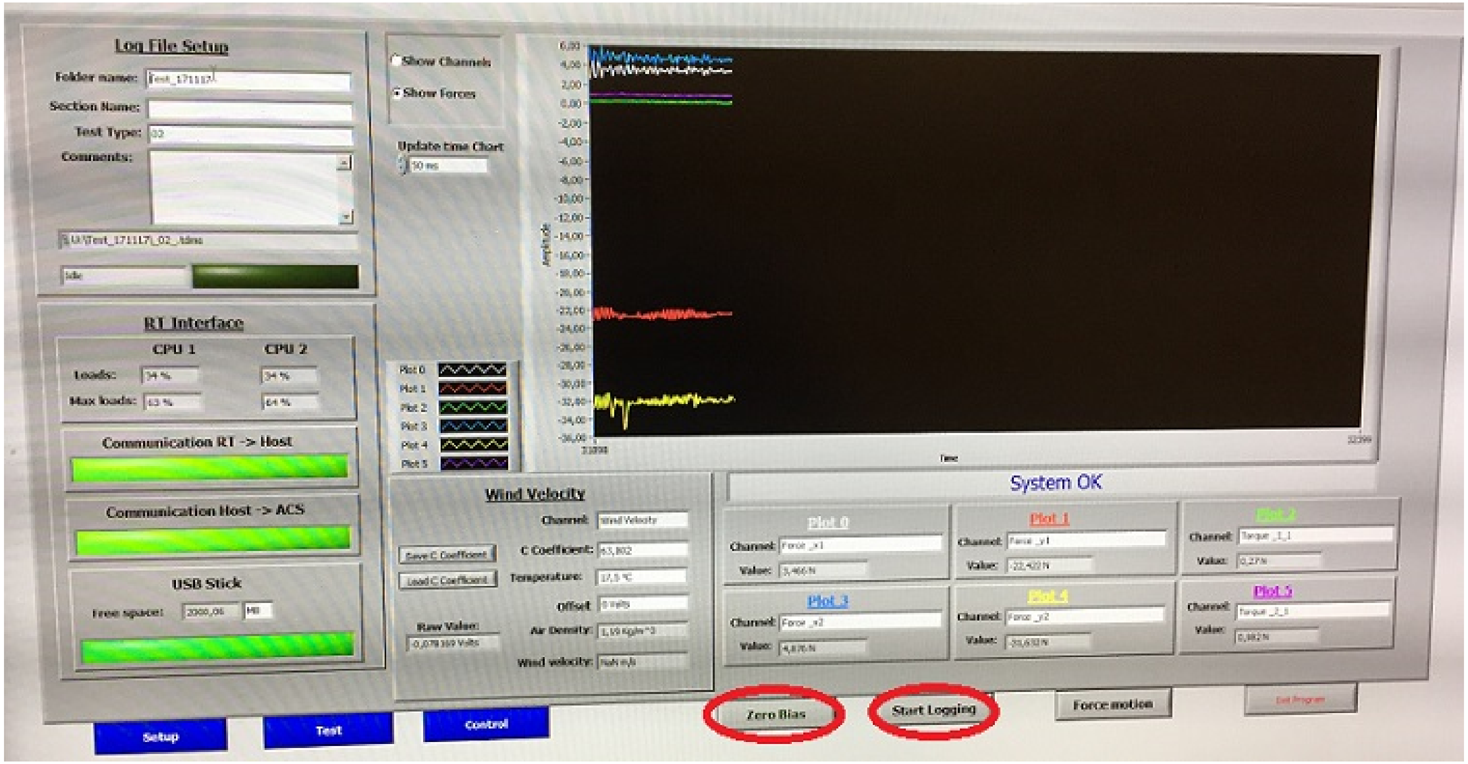

Folder name: Test_171117
Section Name:
Test Type: 02
Comments:
U:\Test_171117_02_.tdms
Idle

○ Show Channels
● Show Forces

Update time Chart: 50 ms

Loads: 34 % 34 %
Max loads: 63 % 64 %

Free space: 2000,06 MB

Channel: Wind Velocity
C Coefficient: 63,802
Temperature: 17,5 °C
Offset: 0 Volts
Air Density: 1,19 Kg/m^3
Raw Value: -0,078 169 Volts
Wind velocity: NaN m/s

Plot 0 Channel: Force_x1 Value: 3,466 N
Plot 1 Channel: Force_y1 Value: -22,422 N
Plot 2 Channel: Torque_1_1 Value: 0,27 N
Plot 3 Channel: Force_x2 Value: 4,876 N
Plot 4 Channel: Force_y2 Value: -31,632 N
Plot 5 Channel: Torque_2_1 Value: 0,082 N

Figure 4.6: User interface of the LabVIEW software.

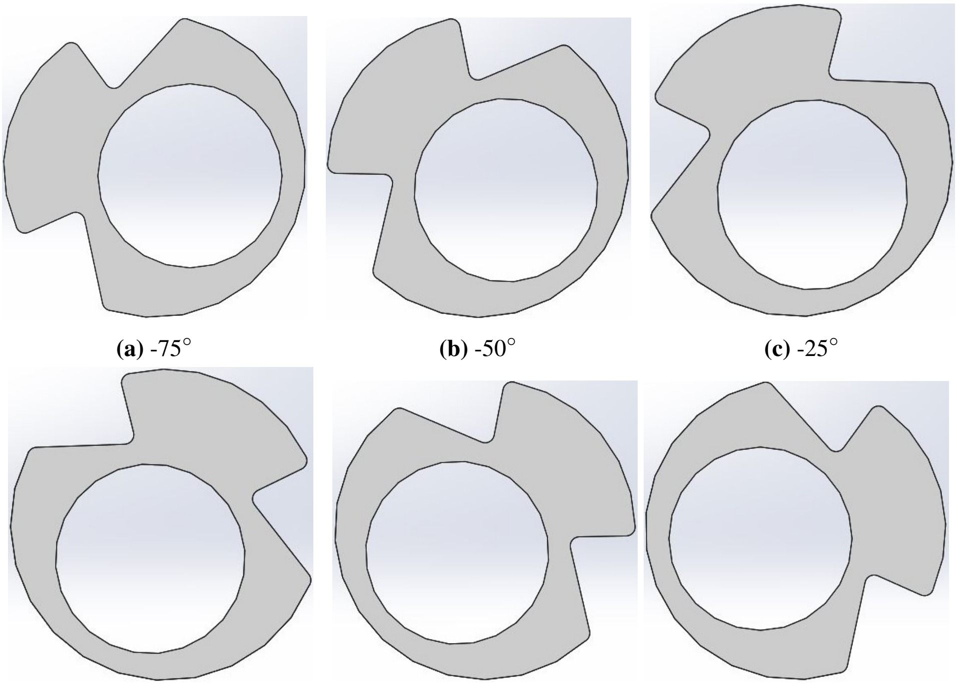

(a) -75° **(b)** -50° **(c)** -25°

(d) 25° **(e)** 50° **(f)** 75°

Figure 4.7: A selection of model rotations to simulate different angles of attack. The wind flow in the tunnel comes in from the left-hand side towards the right.

Bluff bodies can gallop at small flow angles since the flow separation point changes drastically with small changes in angle. Previous wind tunnel tests have included mostly smaller intervals of flow angles, like Stickland and Scanlon (2001) who tested from -10 to 20°. One exception is Xie et al. (2014) who tested between -90 to 90°. This wind tunnel test chose to include an interval in between these two.

The loading cell measurements are in local coordinates which means that the weight distribution of the model changes direction during rotation. A solution to this measurement bias is to reset the system like one does with a kitchen weight. Therefore it's necessary to run the scripts for rotation and measure with zero wind. These data must be subtracted from the measurements with wind flow to remove effects in the loading cells from the weight shift. So the resulting data gives the response influenced by wind.

The measurements for the three wind velocities included the run-up time of the wind tunnel fan. So measurements were started in still air before turning on the wind tunnel. The three scripts for different angles of attack were run after the wind tunnel stabilized around the correct wind velocity.

A natural frequency test was also performed for comparison of the calculations from the model design in chapter 3. The test is a simplified form of an impact test executed with zero wind. One starts measurements and then simply taps on the model to cause a slight vibration, but not to forcefully. The impact causes free vibrations which are measured until they die out. The measurements can be used to identify the natural frequency of the model. Including this, in total 13 measurements were used in the data processing.

4.3 Data Processing

The measurements were taken with a sampling rate of 200 Hz. The data were stored in an excel-file; this file was later converted into a .mat-file by a script written by Ole Andre Øiseth. The .mat-file has a structure with different sections for general properties, measured data and processed data. The properties give the air density and shows the data from user input. The measured data consists of six force components from each loading cell, measured displacements, and measured wind velocities in Volts. The forces, displacements, and flow velocity is SI units must be calculated; this is the processed data.

As mentioned, measurements were taken in still-air to be subtracted from the other data. To do this the two time series must be aligned with each other, since the rotation of the model is performed at different times during the two tests. Following this, the data is put through a low-pass filter. The static coefficients are calculated with equation (2.1), where the drag force is force component 1 plus force component 7, the lift force is component 3 plus 9, and the moment is component 5 plus component 11.

Chapter 5

Description of the Galloping Analysis

A galloping analysis consists of solving the polynomial eigenvalue problem to determine critical wind conditions and system characteristics for an instability to occur. In this case, a critical wind velocity, a critical angle of attack and a critical frequency is to be determined. An instability can happen in a system if the real part of its eigenvalue is positive. The real part of an eigenvalue is an expression including the damping (see equation (2.20)). So if this expression is positive then the damping is also positive. Positive damping means that the systems displacement is increasing; an instability has occurred.

Several factors change the solution of the polynomial eigenvalue problem. The aerodynamic damping and stiffness matrices are a key component to this. These matrices are determined by the slope and mean value of the drag, lift and moment coefficients. These coefficients change for different wind velocities and for different flow angles of attack. Still-air modes of the system are also needed in the analysis. It's therefore necessary to solve the eigenvalue problem considering all these changing variables.

So contributions from an finite element analysis and from the wind tunnel experiment are needed in a galloping analysis. A frequency analysis was performed on a model of a catenary system in Abaqus to determine the still air modes. The still air modes can be used as estimates for the mode shapes in a dynamic analysis. The Abaqus analysis provides the generalized modal system matrices as well. The wind tunnel experiment is relevant for determining the drag, lift and moment coefficients.

5.1 The FE-model

The Abaqus model of a real catenary system is modelled after a railway stretch in Norway. A section of the model is shown in figure 5.1. The model includes a contact wire, stitch wires (16 of them), droppers, and a messenger wire. The length of the stretch is 1260 m. Approximately 1260 m is a common/standard length of a contact wire in Norway (Jernbaneverket (2012)). The transition to the next contact wire is done by an overlap, but this is not included in the model. Table 5.1 shows the cross-section details for the contact wire (CW), messenger wire (MW), stitch wire (SW), and droppers. The choice of using circular cross-sections for e.g. the messenger wire is a simplification which may affect the results. Table 5.2 shows the material constants used. The CuMg02 material is assigned to the droppers, stitch wire and messenger wire. The CuAg01-material is assigned to the contact wire.

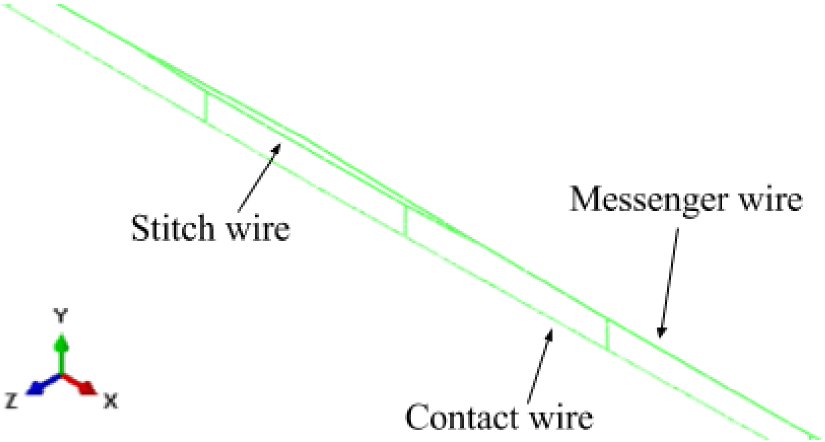

Figure 5.1: A random section from the Abaqus model.

Table 5.1: Cross-section properties

	r [m]	A [m^2]	I$_{11}$ [m^4]	I$_{12}$ [m^4]	I$_{22}$ [m^4]	J [m^4]
CW	-	12.097e-5	1.3442e-9	0	1.1189e-9	1.8446e-9
MW	0.004577	Data generated by Abaqus for circular cross-section				
SW	0.002778					
Droppers	0.001748					

Table 5.2: Materials constants for the FE-model.

		CuAg01	CuMg02
Damping	Alpha	0.062	
	Beta	6.13e-006	
Mass	Density [kg/m^3]	8890	
Elastic	Type	Isotropic	
	Young's Modulus [GPa]	120	108
	Shear Modulus [GPa]	44.78	-
	Poisson's Ratio	0.34	
Expansion	Type	Isotropic	
	Reference Temperature [°C]	20	
	Alpha Coefficient	1.7e-005	

The Abaqus analysis was performed by Petter Røe Nåvik and included a tension and gravity step followed by a frequency step. The tension and gravity step simulates gravity forces as well as the tension put on the system during the building process. This step establishes the correct base for the frequency step. The results from the analysis is written to a .dat-file. The results from the frequency step are used in the galloping analysis. The data were extracted from the .dat-file by using a MATLAB-script developed by Ole Andre Øiseth. Eigenvalue outputs and node outputs were extracted. Eigenvalue outputs include the natural frequencies and the modal mass matrix. The node outputs give the node coordinates of the model and the still air mode shapes.

5.2 The Wind Tunnel Results

Three wind velocities were tested for different angles of attack in the wind tunnel. The galloping analysis uses the real CW-geometry, meaning that the tested velocities are analogous to 20 m/s, 30 m/s and 50 m/s. Linear interpolation was performed to include results for the wind velocities in between. This interpolation provides some error, but it's better to include more velocities than those tested. And the interpolation is not performed outside of the velocities tested, i.e. it doesn't include velocities below 20 m/s or above 50 m/s. The simplification is necessary to be able to perform velocity iterations. The static coefficients were split into a mean and a fluctuating part. This is necessary to calculate the local aerodynamic stiffness and damping matrices.

5.3 Coordinate Transformation

The components of the analysis have different coordinate systems. The static coefficients from the wind tunnel experiment give the aerodynamic damping and stiffness matrices in local coordinates (eq. (2.15c) and (2.15d) in section 2.4), which is represented by the red coordinate system in figure 5.2. The mode shapes from the Abaqus model are in global coordinates. The Generalized equation of motion and the corresponding polynomial eigenvalue problem has to be solved in a global coordinate system. So it's necessary to

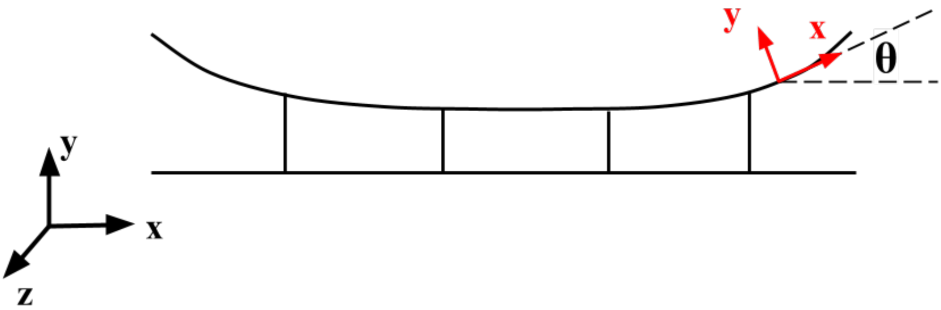

Figure 5.2: Description of the two coordinate systems. Red: local coordinate system, black: global coordinate system.

transform the aerodynamic matrices to the global coordinate system. The transformation between the two systems is done with the rotation matrix, T. In this case, T is defined as shown in equation 5.1. Where $\boldsymbol{r}_L$ and $\boldsymbol{r}_G$ represent the local and global coordinate systems.

$$\boldsymbol{r}_L = T \cdot \boldsymbol{r}_G \qquad T = \begin{bmatrix} cos(\theta) & sin(\theta) & 0 \\ -sin(\theta) & cos(\theta) & 0 \\ 0 & 0 & 1 \end{bmatrix} \tag{5.1}$$

The expression for the global aerodynamic matrices is shown in equation 5.2. Where $T = T(\boldsymbol{x})$, and $\boldsymbol{x}$ is the position along the catenary.

$$K_{ae,global} = T^T \cdot K_{ae,local} \cdot T \tag{5.2a}$$

$$C_{ae,global} = T^T \cdot C_{ae,local} \cdot T \tag{5.2b}$$

5.4 The Solution Method

The criterion in section 2.3.2 indicates galloping. The galloping analysis consists of checking for galloping with the velocities and angles from the wind tunnel experiment, and determining the critical values for onset of galloping. Galloping occurs when the real part of the eigenvalue is positive. The onset of galloping is determined by the lowest damping possible, preferably as close to zero damping as possible. The reason is that this state represents the onset of galloping, when the damping changes sign from negative to positive.

Two different approaches were made to determine critical values for galloping. The first approach was to plot the real part of the eigenvalue (real(s)) vs. the wind velocity with values between 20 and 50 m/s. The second approach was to iterate over wind velocity to identify onset galloping with criteria for the damping (real(s)), CriteriaRe, and for the velocity step, CriteriadV.

The concept of the first approach is that one can determine at what velocity real(s) becomes positive. The analysis was carried out including different still-air modes. Real(s) was calculated and plotted including:

1. Random modes between 1 and 70: mode 1, 2, 4, 7, 10, 11, 16, 17, 23, 24, 30, 31, 32, 40, 45, 47, 51, 53, 55, 58, 59, 60, 62, 65, and 70
2. Random modes between 1 and 297: combination 1 and mode 72, 74, 80, 87, 88, 89, 95, 97, 101, 102, 110, 112, 115, 120, 125, 130, 131, 133, 139, 145, 146, 152, 157, 161, 168, 169, 174, 175, 189, 192, 199, 205, 207, 213, 216, 227, 228, 235, 237, 239, 242, 247, 248, 257, 266, 270, 271, 272, 279, 284, 287, 290, and 297
3. All still air modes, mode 1-297

The second approach iterates over different velocities to find more exact critical values for onset of galloping. This is done including criteria. One criterion for the damping, which should be close to zero. And one criterion for the velocity iteration step, which defines how precise the critical velocity should be, i.e. how many digits included after the decimal point. The analysis was performed for different values and combinations of these criteria. The script checks the polynomial eigenvalue solution calculated for each angle of attack and velocity iteration. The analysis is stopped if real(s) $<$ CriteriaRe, and real(s) $>$ 0, and dv $<$ CriteriadV. If not, a velocity iteration is carried out. The iteration is different depending on if real(s) is positive or not. If real(s) is positive V = V - dV. If real(s) is negative V = v + dV.

The mechanical damping was set to ξ = 0.005, and the density of the air equal to that measured in the wind tunnel.

One source of error is that the messenger wire, droppers and stitch wire are assigned the same static coefficients as the contact wire when determining critical values. The messenger wire, droppers and stitch wire are not included in plotting of the mode shapes.

Chapter 6

Results and Discussion

6.1 Natural Frequency Test

Figure 6.1 shows the time history for the force in the z-direction for one of the loading cells. The three impacts where executed approximately at the 9, 30 and 52 second-marks.

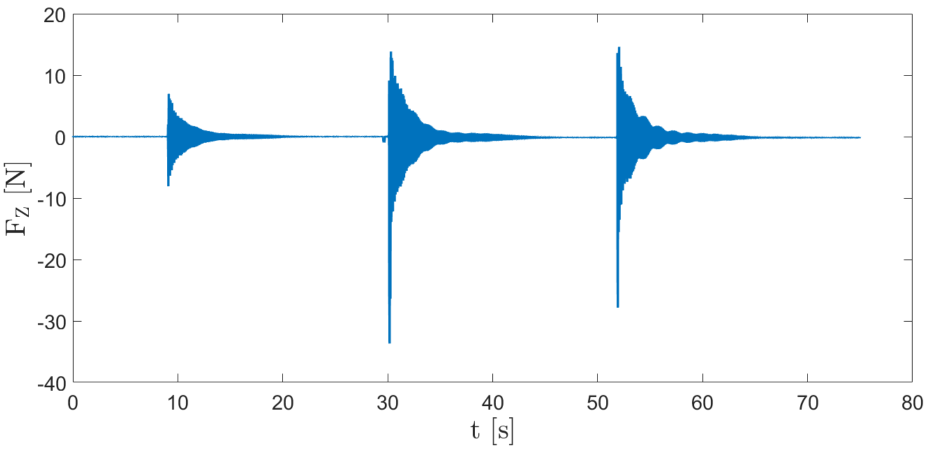

Figure 6.1: Force measurements in z-direction during the natural frequency test

Figure 6.2 shows the spectral density of the forces in the x-, z-, and θ-directions. The vertical peaks are the most interesting in this case considering vortex induced vibration which is in the vertical direction.

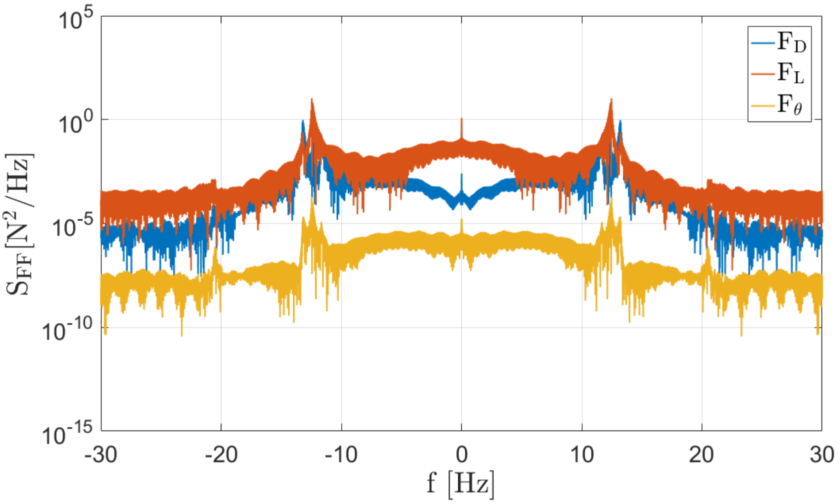

Figure 6.2: Spectral density from natural frequency test

Table 6.1 shows the peaks picked from the spectral density plots in figure 6.2. The fundamental natural frequency is 12.5 Hz. This has been confirmed later on in the process of determining the Strouhal number. The natural frequency from the wind tunnel is close to the natural frequency calculated in chapter 3. The calculation was based on the model being of a Gurit® material instead of the final 3D print. The final model is both heavier and stiffer than the initial design. These characteristics still give a natural frequency close to the calculation which was based on the initial foam material. So the stiffness-weight ratio must be approximately the same for both the initial design and the final model.

Table 6.1: Frequency peaks picked from the spectral density plots [Hz]

Lateral peaks	Vertical peaks	Torsional peaks
11.65	12.47	11.65
12.38	13.21	12.47
13.21		13.21
		20.6

6.2 Strouhal Number

The Strouhal number is determined from the measurement where $\alpha = 0$ and the wind velocity increases from about 0 to 10 m/s. The time series for the wind velocity and the lift force was split into N segments as indicated in figure 6.3. It's noted from figure 6.3 that wind velocities below 4 m/s don't generate significant lift forces. The standard deviation of the lift force for each segment was calculated and plotted. It was plotted versus $\frac{V}{Df}$ which is the inverse of the Strouhal number. V is the mean wind velocity for the segment, D is the diameter of the WT-model and f is the frequency of vortex shedding. The maximum point on the standard deviation- plot is used to determine the Strouhal number (Strømmen (2010)). The Strouhal number was determined for N = 32, 66 and 133. The standard deviation-plot for 133 segments is shown in figure 6.4. Table 6.2 shows the Strouhal numbers calculated from different number of segments.

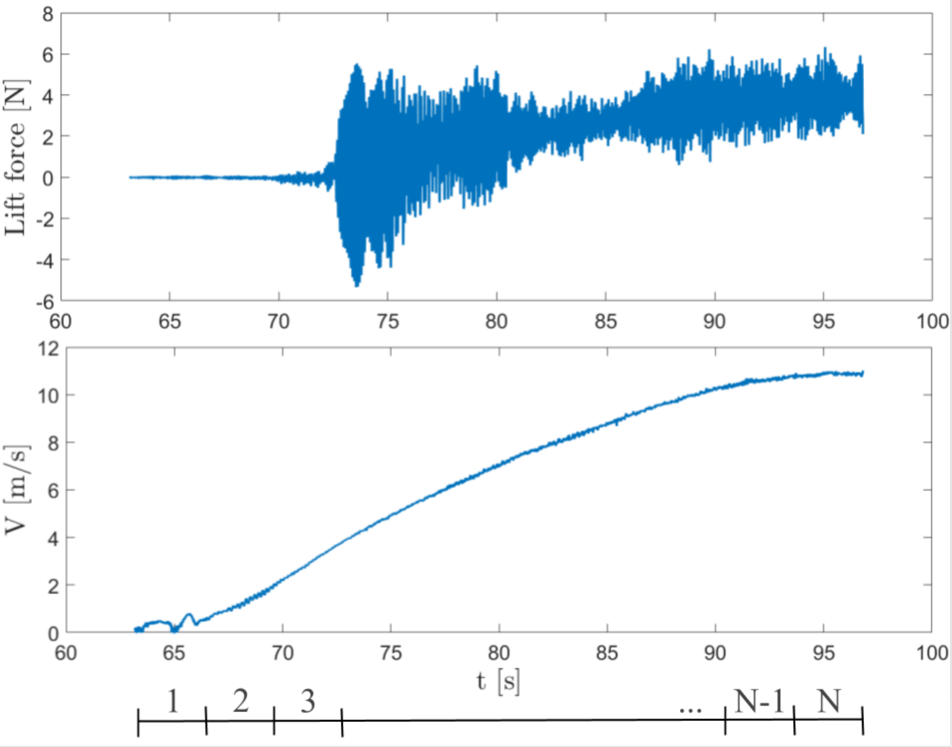

Figure 6.3: Splitting time series into segments.

Table 6.2: Strouhal numbers calculated from different number of divisions

N	Strouhal number
32	0.192
66	0.197
133	0.194
Mean	0.194

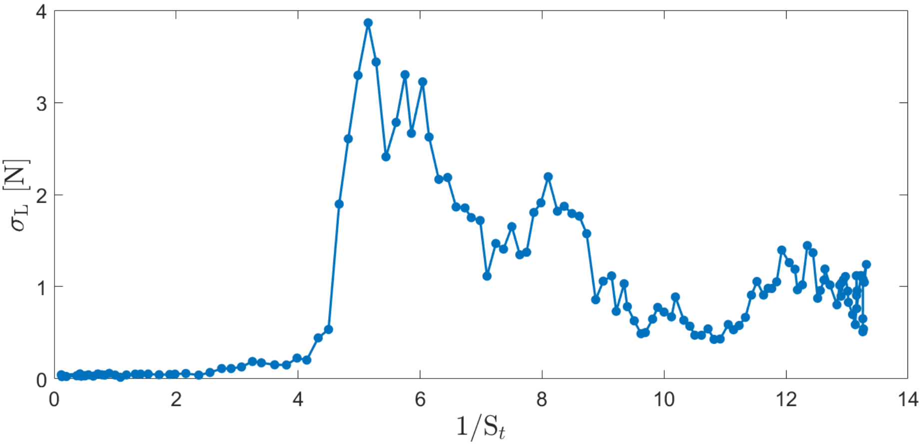

Figure 6.4: Standard deviation of the lift force vs. the inverse Strouhal number

The largest N provides the most accurate Strouhal number. One can see from figure 6.3 that the wind tunnel fan accelerates from 0 to 10 m/s in about 30 seconds. The mean velocity is the basis of the calculation of the Strouhal number. The maximum standard deviation is plotted against $\frac{V}{Df}$ where V is the mean wind velocity. So, a larger number of divisions gives a more precise mean wind velocity for each segment which in turn gives a more accurate Strouhal number. The standard deviation of the lift force for N = 133 is shown in figure 6.4. The largest N gives the Strouhal number as $S_t = 0.194$. The mean of all calculations is the same.

Spectral density plots confirm the natural frequency of the WT-model by demonstrating the lock-in effect. Spectral densities for selected segments for N = 32 are shown in figure 6.5. The behaviour is dominated by a single frequency when the wind velocity is between 3.7573 and 4.7695 m/s. The dominant frequency is the frequency of oscillation. Lock-in occurs when the frequency of oscillation is equal to the shedding frequency. In other words, when the natural frequency of the WT-model is equal to the shedding frequency. So lock-in vibration at 12.5 Hz confirms the natural frequency determined in section 6.1.

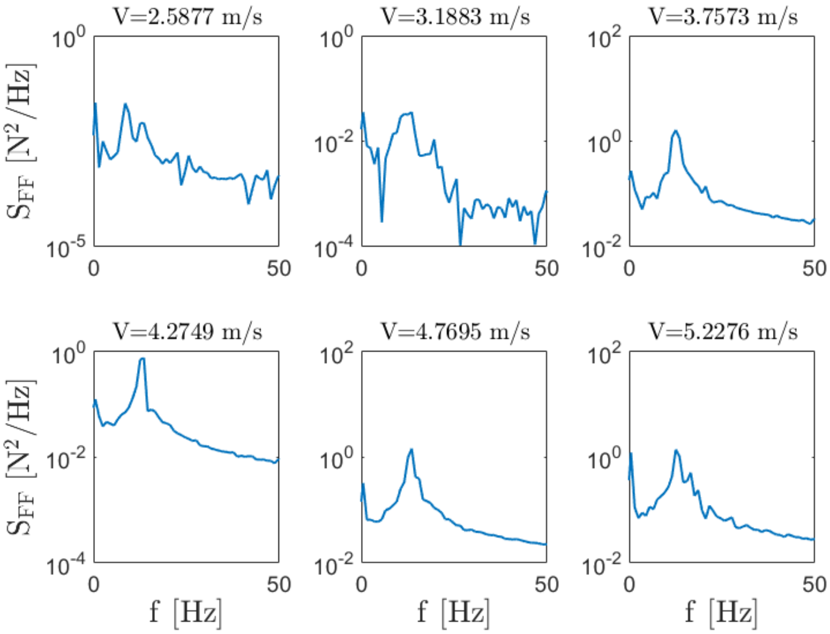

Figure 6.5: Spectral density of the lift force for selected segments around lock-in

6.3 Drag, Lift and Moment Coefficients

Following are the plots for the drag, lift and moment coefficients plotted against angle of attack and Reynolds number. The plots for different angles of attack show all measurements made, so there's multiple measurements at all angles of attack. The legends describe the wind tunnel velocities. Real life velocities for an unscaled contact wire are respectively 20, 30 and 50 m/s.

Coefficients vs. Angle of Attack

Figure 6.6 shows the drag coefficients calculated from the wind tunnel tests. One can see that the graphs for 6 and 10 m/s show more of the same tendencies, than that for 4 m/s. The reason for this is most likely because of the vortex-induced vibrations at 4 m/s. The drag coefficient decreases with increasing wind velocity, as is also the tendency in the report by Xie et al. (2014). The scaling is 2:1 in this report which makes the values a bit different, the cross-section tested is AC-150 not AC-120. The drag coefficient at 10 m/s (20 m/s with real CW) in Xie et al. (2014) is most comparable to the drag coefficient at 4 m/s (20 m/s for real CW) in this report. They have the same value at -75° which is about 1.3. But the other values differ, possibly because of the vortex-induced vibrations which occurred in the testing for this report.

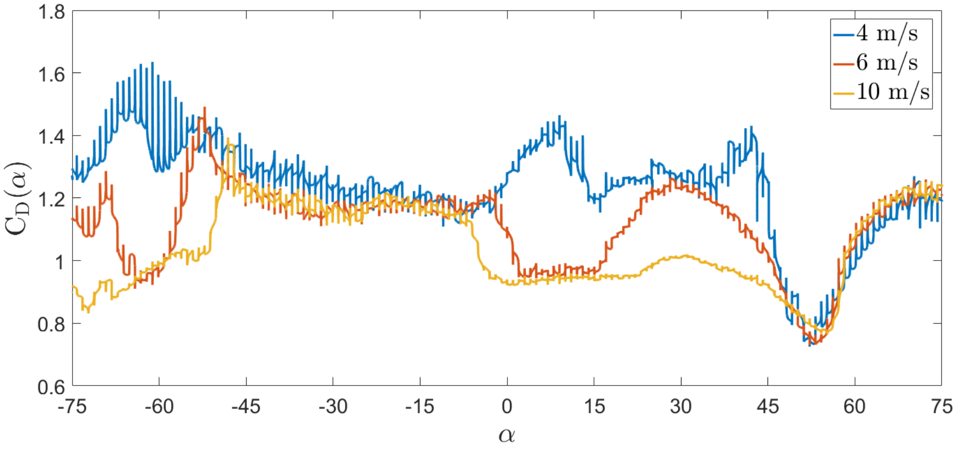

Figure 6.6: Drag coefficient for different wind tunnel velocities

Minimum drag is for α equal to approximately 50° for all velocities tested. Maximum drag is for a negative angle of attack. For WT-velocity 4 m/s at $\alpha \simeq$ -65°. For 6 m/s at $\alpha \simeq$ -55°. And for 10 m/s at $\alpha \simeq$ -50°. So, the point of maximum drag shifts towards more positive angles of attack with increasing wind velocity.

Figure 6.7 shows the lift coefficients calculated from the wind tunnel tests. All graphs for the lift coefficient seem to have the same tendencies except for a discrepancy between about 0 and 15 degrees. The question is why the measurement at 4 m/s differs more from the other velocities for drag than it does for lift when it comes to following tendencies for maximums and minimums. The velocities of 6 and 10 m/s have almost the same extremal

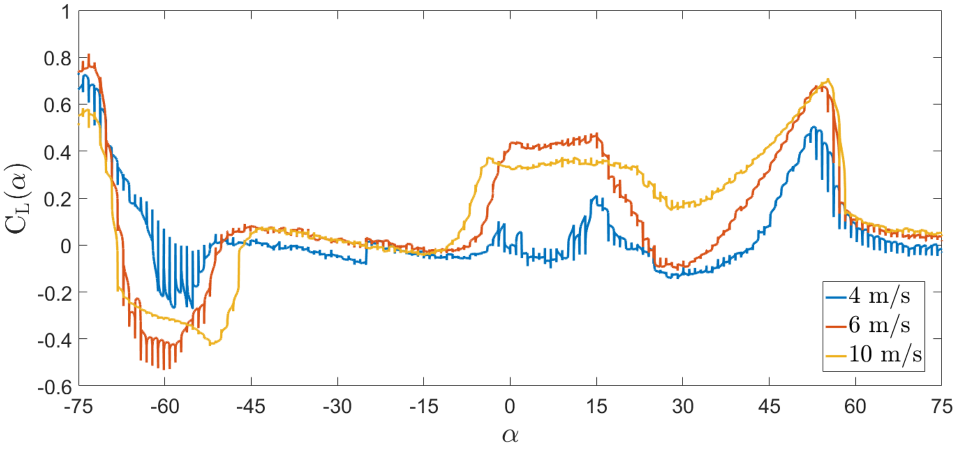

Figure 6.7: Lift coefficient for different wind tunnel velocities

points. It might be that the vortices push the cross-section in the opposite lateral direction when they're shed, so that the drag coefficient deviates from the other measurements.

Increased wind speed leads to increased magnitude of lift at several angles. The opposite is also observed, but this happens at angles where the different velocities give different directions of lift. All velocities give negative lift somewhere between $\alpha = -70°$ and $\alpha = -45°$. After this it's mostly the measurements for V = 4 m/s which exhibits a small value of negative lift. Different directions of lift at different velocities occurs because of changes in the position and size of the wake. The wake is the area behind the flow separation point. Different velocities gives different pressure distributions downstream, therefore different magnitude of lift. Different velocities can also cause a new point of reattachment, which shifts the wake in a new position above or below the body causing a change in direction of lift. Changes in sign can cause galloping Tamura and Kareem (2013).

Maximum lift for V = 4 m/s and V = 6 m/s occur at an angle of attack approximately equal to -75°. Maximum lift for V = 10 m/s is at angle of attack approximately equal to 55°.

The lift coefficient is asymmetric about the y-axis as is expected because of different presence of grooves. For example an angle of attack equal to 75° hides the grooves from the oncoming flow. But in spite of different groove-placements, there is significant peaks at both -60° and 60°. The absolute value of the lift coefficient is a bit larger for $\alpha = 60°$. There are larger lift coefficients for positive angles in general. Positive angles of attack give positive lift, some negative angles of attack give negative lift. This is because the groove facing the flow is directed downward at negative rotations. The positive angles of attack provide more area of resistance to the flow in the upwards vertical direction, with the groove directed upwards.

Figure 6.8 shows the pitching moment coefficients calculated from the wind tunnel tests. The moment coefficient increased with increasing velocity for negative angles of attack and decreased for increasing velocity at positive angles of attack.

It can be observed from figure 6.6-6.8 that the coefficients have a greater 'span' at different angles of attack when the wind tunnel velocity is 4 m/s. This is because the critical velocity for vortex-induced vibration is approximately equal to 4 m/s. This leads to a larger variation in deflection which leads to a larger variation in the forces measured by the loading cells. Wind tunnel testing at velocities close to and around the critical values for vortex shedding are usually avoided for determining static coefficients. But it's necessary for determination of the Strouhal number. The scaling of the model and the desired wind velocity interval made it difficult to avoid a vortex-induced instability when testing to determine static coefficients. Wind velocities in Norway rarely exceed 30 m/s (NRK and MET Norway (2013)) and it was therefore of interest to test wind velocities below and up to 30 m/s. A diameter-scaling of 5:1 changes 30 m/s to 6 m/s in the wind tunnel tests. This value is low and measurements at even lower velocities (e.g. 3 m/s) were expected to be poor. The reason for this is that the loading cells wouldn't be able to measure the

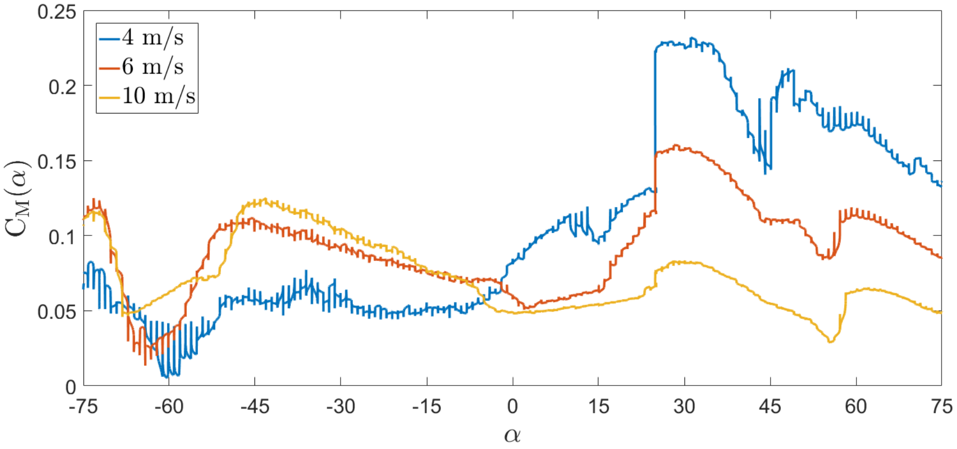

Figure 6.8: Moment coefficient for different wind tunnel velocities.

corresponding low forces very well. It was not desired to test for wind velocities lower than 4 m/s. And since it was of interest to test a velocity below 6 m/s the measurements at 4 m/s were performed. The measurement at WT-velocity of 10 m/s was also performed to see the response at higher velocities. This corresponds to 50 m/s on a real life contact wire.

A confirmation of the results is the values of the coefficients at the angle of attack, $\alpha = 75°$. The part of the model facing the flow is equal to that of a cylinder. One can see from figure 6.6 that the value of C_D is approximately equal to 1.2 at this angle of attack, and from figure 6.7 that the value of C_L is equal to zero. A cylinder doesn't experience lift and 1.2 is the drag coefficient of a cylinder (Cengel and Cimbala (2006)).

The drag and lift graphs are almost identical at certain angles of attack, e.g. between -45 to -5°. This is because some angles of attack introduce the corners of the grooves to the flow, causing separation no matter what the Reynolds number is. Also between angles of 50 to 75° the contact wire is ”hiding” the grooves, so the area facing the wind is cylindrical, and the velocities all give roughly the same drag and lift coefficients.

There is a big jump in the C_M graph for 4 and 6 m/s when going from measurement -25-25 to measurement 25-75. The jump decreases with increasing wind tunnel velocity. The reason for the jump could be that the values of the moment coefficients are low. This means that the loading cells measure very low forces which makes the measurements more unreliable.

The lift, drag and moment coefficients are difficult to compare to other research. It's difficult to compare the measured moment coefficient to other measurements since most research papers only include the drag and lift coefficients. And it's difficult to compare the drag and lift coefficients because most research papers communicate their results in the Glauert-Den Hartog Stability Criterion. The criterion is the most important manifestation of the results in practice. The moment coefficient is not included in the mentioned stability criterion.

Changing alpha leads to a change in the boundary layer of the flow around the body. The flow will separate from the surface at different points when changing the angle of attack of the flow. The contact wire cross section is circular. Flow separation occurs at high curvature which means that the contact wire is highly vulnerable to the effects of flow separation. The grooves are also a trigger for flow separation. The flow separation creates a pressure difference with higher pressure downstream of the separation point. The separated region, also known as the wake, contributes to the static coefficients. Early separation cause a larger wake area which is less steady (turbulent) and can cause fluctuations. Flow separation is dependent on Reynolds number, turbulence and surface roughness. The grooves on the contact wire changes the flow separation point. The grooves can also cause separation bubbles which means that the flow separates then reattaches later on. Tamura and Kareem (2013).

Coefficients vs. Reynolds Number

Figure 6.9 shows the drag coefficient at $\alpha = 0$ plotted for different Reynolds numbers. The Reynolds number is calculated from velocities of 4.0 m/s up to 10.9 m/s.

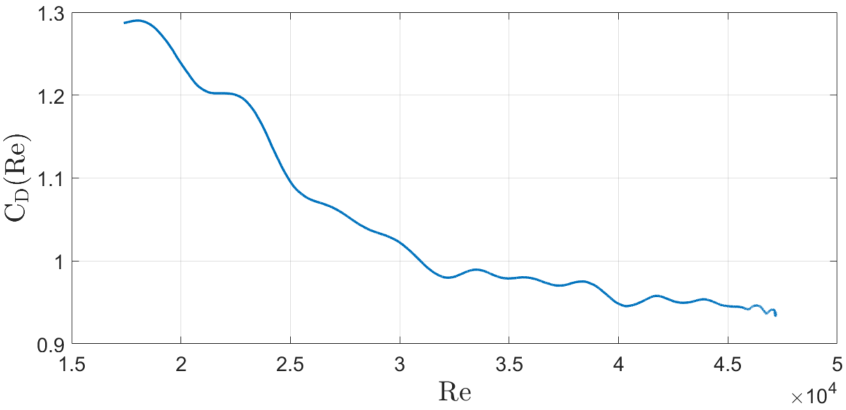

Figure 6.9: Drag coefficient vs. Reynolds number at α = 0°

It seems like the drag coefficient has reached Reynolds number independence. One can see from figure 6.9 that the drag coefficient decreases with increasing Reynolds number, which was also evident at most angles of attack in figure 6.6. This is because of reduced flow separation, the separation occurs further back on the cross section, which makes the wake smaller. The smaller wake has higher pressure than a larger wake, which reduces the drag by behaving as an opposite force. The measured drag coefficient seems to stabilize around $C_D \simeq 1$. The measurements stop at Reynolds number below 2e5 so it's not possible to see if a drop will occur like it does for cylinders at Re = 2e5 (drop from 1.2 to 0.3). This drop could occur earlier for a certain angle of attack on a contact wire, but the ups and downs on figure 6.6 aren't as extreme as the drop on a cylinder. Also, the effect of the grooves are not directly comparable to the effect of the Reynolds number and surface roughness on a cylinder.

Figure 6.10 shows the lift coefficient at $\alpha = 0$ plotted for different Reynolds numbers. The lift coefficient might have reached Reynolds number independence. The coefficient experiences an increase in lift as the Reynolds number increases. This is followed by a region where the lift is reduced before it seems to stabilize at $C_L \simeq 0.3$. The turning point is at $Re \simeq 2.5e4$. Change in wake because of flow separation and reattachment can effect the lift. The lift can change rapidly with different positions of reattachment, both with respect to magnitude and direction. The increase in positive lift is a result of increased pressure at the bottom of the cross-section. This can be a result of the flow separation point being placed further back on the bottom of the cross-section than on the top, so that the wake is oriented towards the top. The wake has lower pressure. The top of the contact wire has grooves which can interrupt trailing edge flow, while the bottom is circular so the flow can follow the cross-section surface further along.

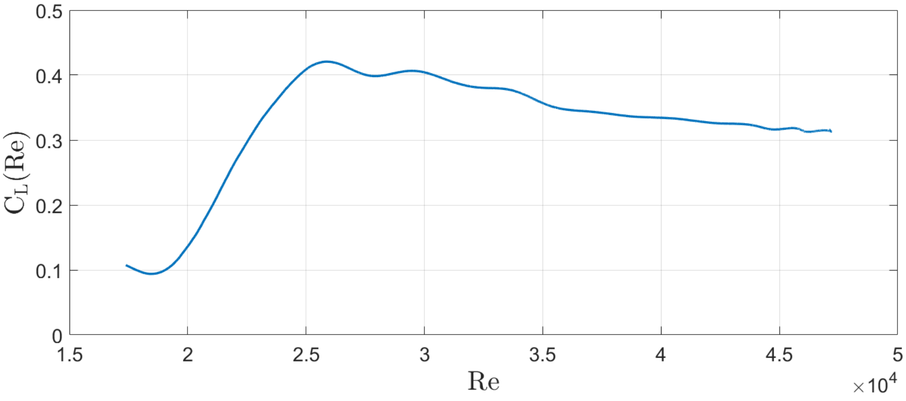

Figure 6.10: Lift coefficient vs. Reynolds number at α = 0°

Figure 6.11 shows the moment coefficient at $\alpha = 0$ plotted for different Reynolds numbers. The moment coefficient has also reached Reynolds number independence.

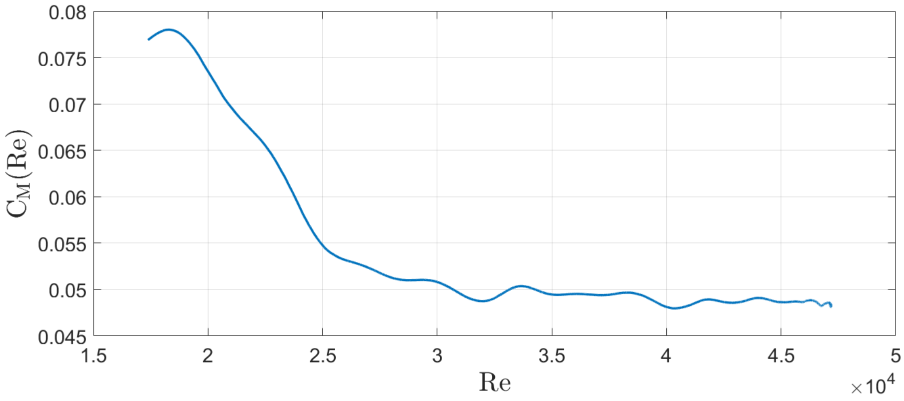

Figure 6.11: Moment coefficient vs. Reynolds number at α = 0°

6.4 The Glauert-Den Hartog Stability Criterion

Figure 6.12 shows the Glauert-Den Hartog Stability Criterion for the wind velocities tested in the wind tunnel. The values were determined at all integer angles of attack. So part of the calculation was to find the mean of the static coefficients at all flow angles. Figure 6.13 shows the stability criterion for V = 4 m/s. One can see from figure 6.13 that the stability criterion varies significantly more than for the other wind velocities and has a more messy nature (vortex-induced vibration). Figure 6.14 shows the stability criterion for V = 6 m/s. Figure 6.15 shows the stability criterion for V = 10 m/s.

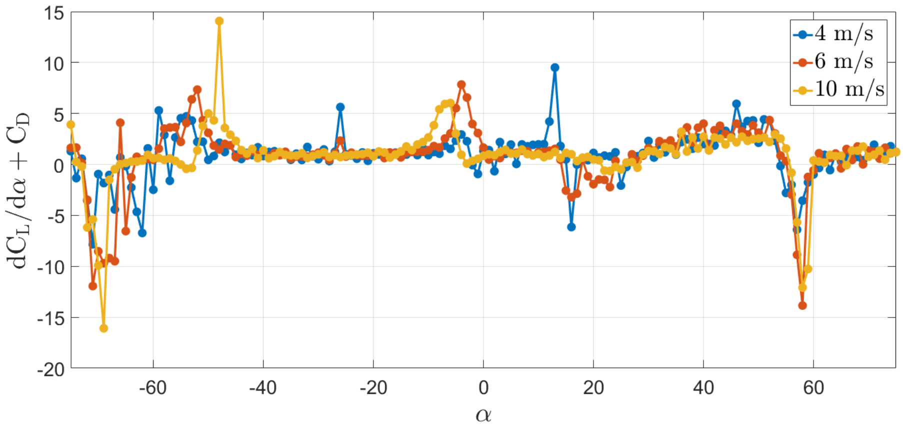

Figure 6.12: The Glauert-Den Hartog Stability Criterion for different wind tunnel velocities

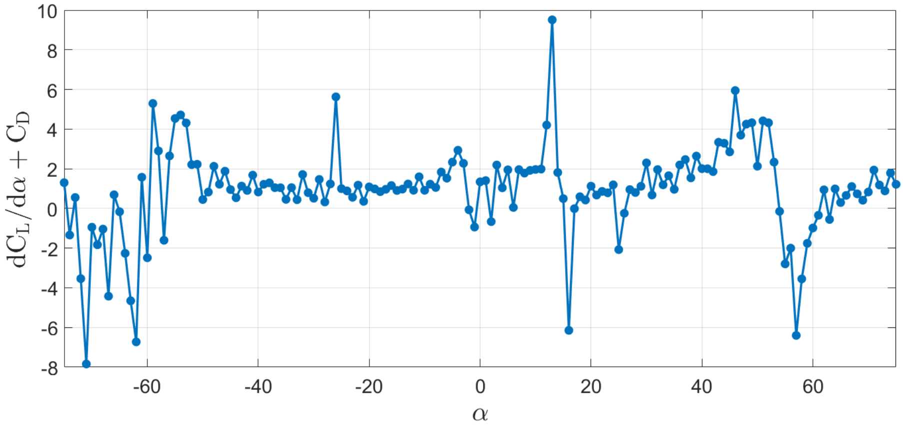

Figure 6.13: The Glauert-Den Hartog Stability Criterion for V = 4 m/s

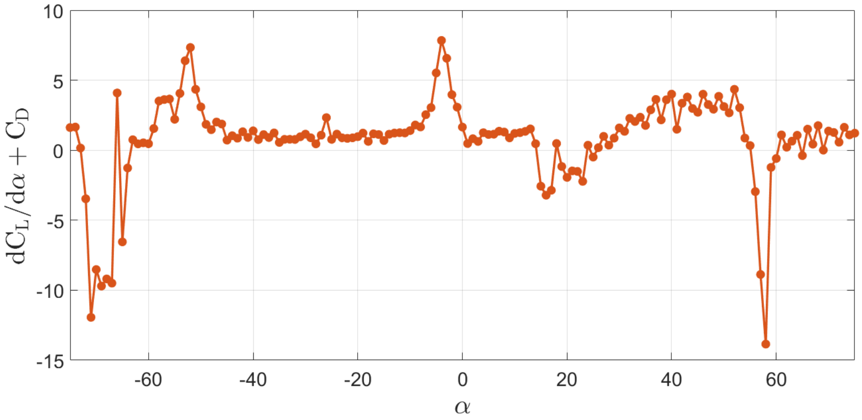

Figure 6.14: The Glauert-Den Hartog Stability Criterion for V = 6 m/s

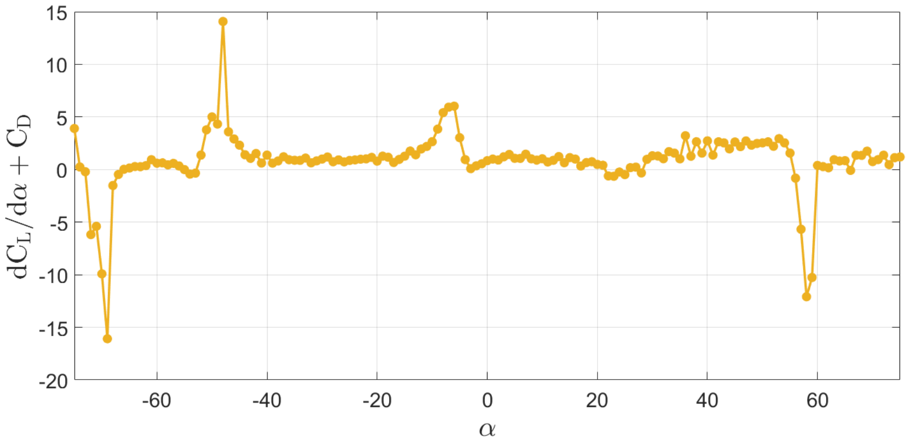

Figure 6.15: The Glauert-Den Hartog Stability Criterion for V = 10 m/s

It can be seen that the stability criterion $d = \frac{dC_L}{d\alpha} + C_D$ is significantly less negative for increasing velocity. $d < 0$ the most for V = 4 m/s, but this is expected because of the vortex shedding. The danger of galloping is present for V = 6 m/s which equals 30 m/s for a real contact wire. A wind velocity of 30 m/s is defined as a violent storm on the Beaufort scale, and rarely occurs on land in Norway. This velocity in the mountains is followed by closing roads and railway lines. The WT-results at 10 m/s are for real life wind velocities at 50 m/s, which is classified as hurricane. Hurricane conditions very rarely occur in Norway (NRK and MET Norway (2013)). But if they occur, there's a probability of galloping at 50 m/s at certain angles of attack. There's also a danger of galloping at wind velocities between 30 and 50 m/s not tested here.

6.5 Galloping Analysis on a Real Catenary System

6.5.1 Approach 1: Plotting Real(s)

The three different combinations used in the analysis were:

1. Random modes between 1 and 70: mode 1, 2, 4, 7, 10, 11, 16, 17, 23, 24, 30, 31, 32, 40, 45, 47, 51, 53, 55, 58, 59, 60, 62, 65, and 70

2. Random modes between 1 and 297: combination 1 and mode 72, 74, 80, 87, 88, 89, 95, 97, 101, 102, 110, 112, 115, 120, 125, 130, 131, 133, 139, 145, 146, 152, 157, 161, 168, 169, 174, 175, 189, 192, 199, 205, 207, 213, 216, 227, 228, 235, 237, 239, 242, 247, 248, 257, 266, 270, 271, 272, 279, 284, 287, 290, and 297

3. All still air modes, mode 1-297

The calculation and plotting takes a long time when including all still air modes (combination 3). The challenge is to decide which modes to include for an efficient analysis. Only angles of attack with positive real(s) were plotted.

Table 6.3 shows the results from the calculation. Combination 1 and 2 give the same results, and almost identical plots. Combination 3 is quite different. The combination excludes some of the angles from 1 and 2, and it introduces a lot of new critical angles and velocities. Combination 3 gives curious results when one compares it to the Glauert-Den Hartog stability criterion. It introduces some angles which are not unstable according to the criterion, e.g. α's between -50 and -34, as well as between 38 and 48. Although, it's worth noting that the criterion is close to zero at these angles. Some of these curious results also note ”stable after 30”, which indicates that maybe they only appear because of the vortex shedding during WT-testing. Combination 3 changes some of the critical velocities at certain angles as well, e.g. at $\alpha = 59°$.

One example of a plot for the angles of attack who note ”stable after 30” is shown in figure 6.16. The plot is taken from combination 1 and is similar for α = -74, -63, -60 and -57°. α = 25 and 55° are a bit different, but have the same tendency. The plot indicates that the measurement at 20 m/s (WT-velocity 4 m/s) can be unstable.

Table 6.3: Critical angles and velocities for combination 1, 2 and 3.

Combination 1 and 2			Combination 3		
α_{CR} [°]	V$_{CR}$ [m/s]	Notes on real(s)	α_{CR} [°]	V$_{CR}$ [m/s]	Notes on real(s)
-74	20	stable after 30	-73	20	stable after 30
-72	20	always positive	-72	20	stable after 30
-71	20	always positive	-70	20	always positive
-70	21	still unstable at 30	-69	20	always positive
-69	20	always positive	-68	20	always positive
-68	20	always positive	-67	20	always positive
-67	20	still unstable at 30	-65	20	always positive
-65	22	still unstable at 30	-64	20	still unstable at 30
-64	20	still unstable at 30	-62	22	still unstable at 30
-63	20	stable after 30	-61	20	always positive
-62	20	stable after 30	-60	20	still unstable at 30
-60	20	stable after 30	-59	20	always positive
-57	20	stable after 30	-58	20	always positive
15	25	still unstable at 30	-57	20	stable after 30
16	20	still unstable at 30	-56	20	always positive
17	24	still unstable at 30	-55	20	always positive
19	28	still unstable at 30	-54	20	still unstable at 30
20	27	still unstable at 30	-52	22	still unstable at 30
21	28	still unstable at 30	-51	20	still unstable at 30
22	28	still unstable at 30	-50	20	stable after 30
23	26	still unstable at 30	-49	20	stable after 30
25	20	stable after 30	-48	20	stable after 30
55	20	stable after 30	-46	20	stable after 30
56	20	always positive	-43	20	stable after 30
57	20	always positive	-34	46	
58	20	always positive	16	20	stable after 30
59	20	always positive	20	20	stable after 30
			38	25	still unstable at 30
			39	20	still unstable at 30
			40	24	still unstable at 30
			42	29	still unstable at 30
			43	27	still unstable at 30
			44	28	still unstable at 30
			45	28	still unstable at 30
			46	26	still unstable at 30
			48	20	stable after 30
			59	46	

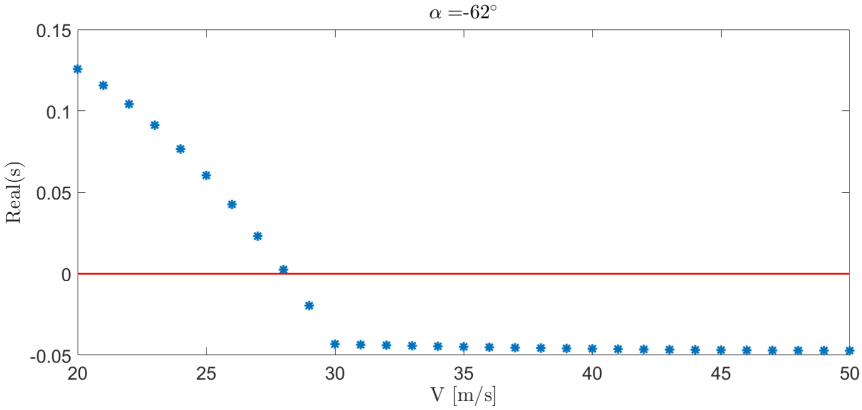

Figure 6.16: Plot of real(s) for $\alpha = -62°$. Combination 1.

Several plots have similar shape to that shown in figure 6.17. The shape is similar for $\alpha =$ -71, -68, -67, -65, 17, 19, 20, 21, 22, 23 and 56°. These have the note ”still unstable at 30” and ”always positive”.

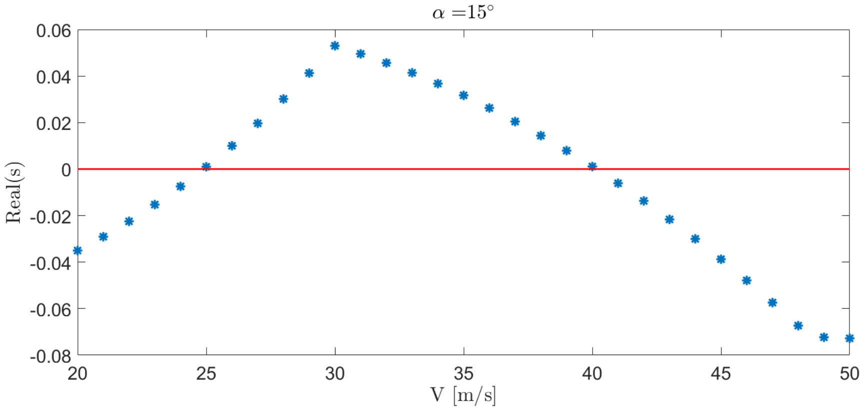

Figure 6.17: Plot of real(s) for $\alpha = 15°$. Combination 1.

A plot worth mentioning is the one for $\alpha = 59°$ for combination 1 (fig. 6.18). Real(s) is always positive, but stays at a low value until it reaches V = 30 m/s, and it grows rapidly. One possible conclusion of this is that the critical velocity at $\alpha = 59°$ is $V_{CR} = 30m/s$, since the measurements below form a straight line, and then increases from 30 m/s.

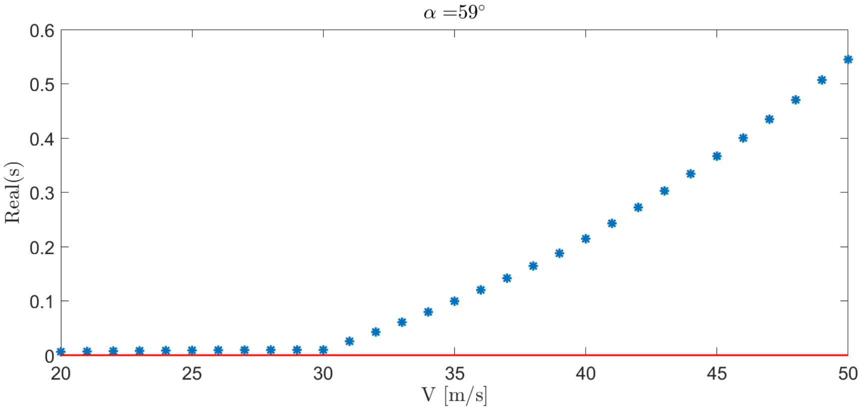

Figure 6.18: Plot of real(s) for $\alpha = 59^\circ$. Combination 1.

Figure 6.16-6.18 are for combination 1 and 2. Figure 6.19 how different the plots can be for combination 3. The angle of attack equal to 59° is stable until V = 46 m/s with combination 3.

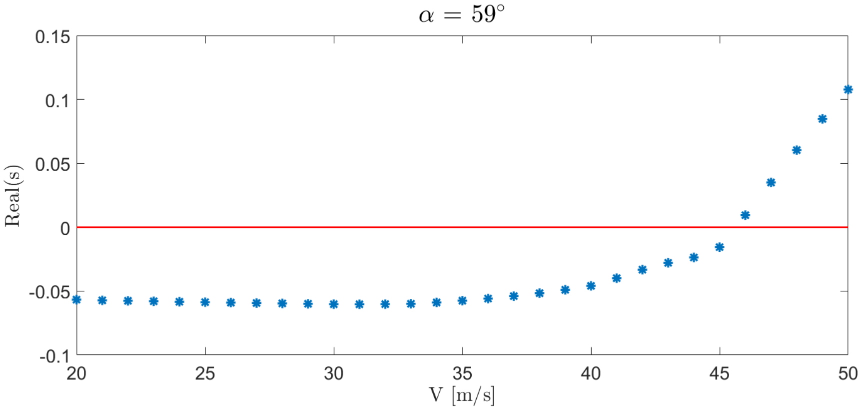

Figure 6.19: Plot of real(s) for $\alpha = 59^\circ$. Combination 3.

Mode Shapes

A critical velocity and its angle of attack gives many eigenvalues and mode shapes. The interesting mode shape out of these is the one for minimal, positive damping, i.e. the mode shape for the eigenvalue where real(s) has the lowest, positive damping.

Note that the mode shapes are highly distorted since the FE-model is 1260 meters long, and mode shapes are plotted for this length. The FE-model has 19 bracket-nodes within the span, so 20 sections in total over 1260 meters. So, a drawn mode shape looks like it has a lot of half waves, but in reality there's not many half waves per section.

One assumption is that the mode shapes for galloping velocities will show cross-wind movement. Galloping is often called cross-wind galloping (Dowell (2014)). For example at very large angles of attack the mode shape is assumed to be mostly lateral since the flow is almost vertical, see figure 6.20 for illustration. This might be correct in some cases, but in reality there are many factors that affect the direction of movement in the catenary system, not just the direction of the flow. The direction of flow affects the movement when considering the grooves. The contact wire isn't circular so the grooves may change the direction at different α. The flow direction doesn't change the fact that the catenary system consists of many restrictions. The Abaqus model is for a contact wire of length 1260 m, where several support poles are present as boundary conditions. The boundary conditions limit the movement. So, the mode shapes may not follow the assumption on cross-wind movement. But a large angle of attack may give a larger lateral contribution than a small angle of attack.

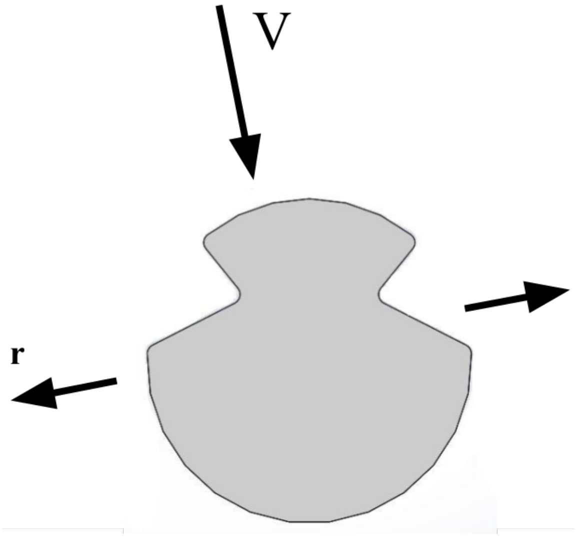

Figure 6.20: Assumed movement at $\alpha = -75°$.

Table 6.4 shows the nature of the mode shapes for all critical angles of attack and their critical velocities. The α's in table 6.3 that are still unstable at 30 m/s have two mode shapes, one for V $<$ 30 m/s and one for V $=$ 30 m/s. Although there's reason to believe that the measurement at 20 m/s is unreliable one can't rule out that some of the critical velocities for certain angles of attack are close to 20 m/s. Some might be low since the catenary system has relatively low mechanical damping (Kaczinski (1998)). Many of the mode shapes were found in the FE-model. The mode shapes in table 6.3 have a critical frequency which was compared to the frequency of the still-air modes. Shape was also evaluated in the comparison. The details of the comparison can be seen in appendix B.

There is no obvious pattern when it comes to mode shape direction and angles of attack. Both large and small angles of attack give vertical mode shapes. But the smallest angles of attack, 15-17° have mode shapes with mostly vertical components, which coincides with the cross-wind mode shape assumption. And the mode shapes denoted "Vertical and lateral" are represented by mostly larger angles of attack(except for $\alpha = 20°$ for combination 1 & 2), which can also be roughly cross-wind movement.

Table 6.4: Mode shapes for different critical velocities and angles of attack

	Combination 1 & 2		Combination 3	
Mode shape	V_{CR}	α_{CR} [°]	V_{CR}	α_{CR} [°]
Vertical	20	-74, -72, -69, -68, -67, -64, -63, -60, -57, 55, 58, 59	20	-73, -72, -69, -68, -67, -65, -64, -60, -57, -50, -49, -43, 20
	24	17	30	-62, -61
	25	15		
	26	23		
	27	20		
	28	21, 22		
	30	15, 16, 17, 19, 20, 21, 22, 56, 59		
Vertical, small lateral	20	-62, 16, 25, 57	20	-70, 16
	30	-72, -65	22	-62
			30	-64, -65
Lateral	30	-70	20	-61, -59, -58, -56, -55, -54, -51, -48, -46, 48
			22	-52
			24	40
			25	38
			27	43
			28	44, 45
			29	42
			30	-70, -59, -58, -55, -54, 38, 39, 40, 42, 43, 44, 45, 48
			46	-34
Vertical and lateral	20	-71, 56	20	39
	21	-70	26	46
	22	-65	30	-69, -68, -67, -60, -56, -52, -51, 46
	30	-71, -69, -68, -67, -64, 21, 57, 58	46	59

The following figures show some of the mode shapes encountered. Figure 6.21 shows a vertical mode shape that appears three times for combination 1 & 2 with α equal to 15, 19 and -68°. It appears nine times for combination 3 with α ranging from -43 to -73° as well as $\alpha = 20°$. The mode shape is identical to still-air mode shape 1 in the Abaqus model.

Most of the mode shapes denoted ”Lateral” are like the one shown in figure 6.22. The mode in figure 6.22 appears a total of 29 times for combination 3, raising the question of whether it’s an actual problem or a numerical error. It could be a numerical error since many of the angles of attack associated with the mode are not critical in the Glauert-Den Hartog stability criterion (fig. 6.12). The modes in figure 6.22 are equal to still-air mode 61 and 62. Combination 3 includes still-air mode 61 which is not present in combination 1 & 2, this might cause a numerical error. If the mode shape represents an instability, it’s only present in one section between two support poles. It’s the second section from the end for both modes. The FE model has 20 sections. The support poles are not included, but there’s 19 nodes representing the contact point between the messenger wire and the brackets.

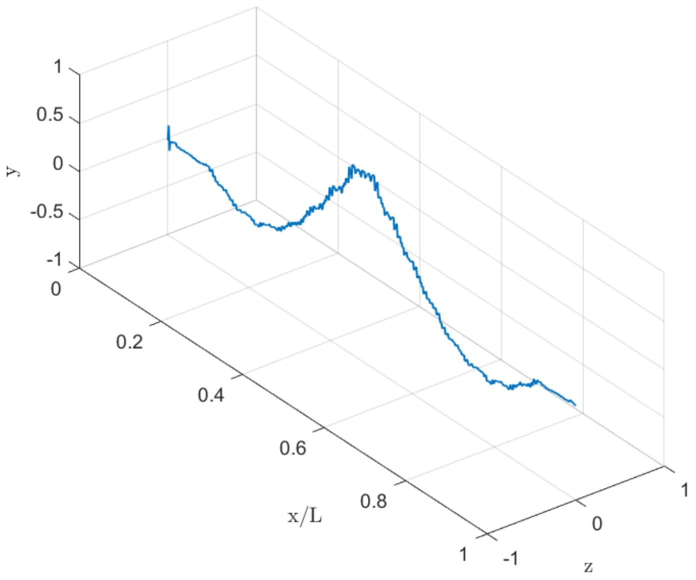

Figure 6.21: Vertical mode shape. Appears three times for combination 1 & 2, nine times for combination 3. The mode shape is the same as still-air mode 1 in the FE-model.

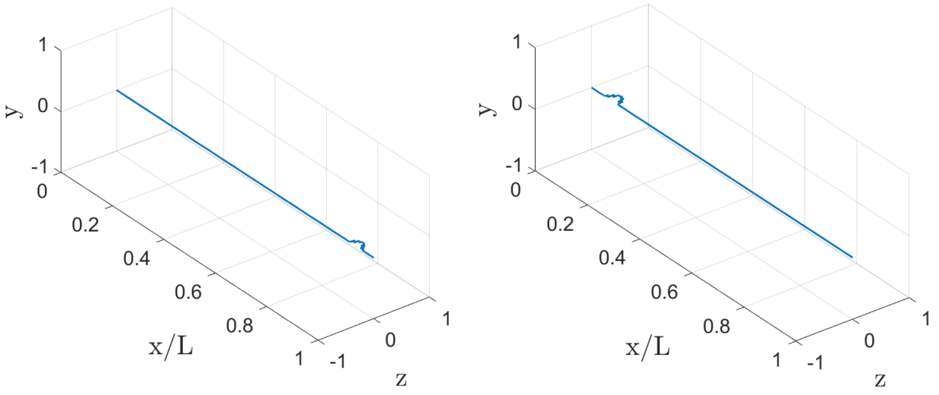

(a) Mode shape equal to still-air FE-mode 61.

(b) Mode shape equal to still-air FE-mode 62.

Figure 6.22: Mode shape that appears a lot for combination 3 (29 times), and once for combination 1 & 2.

One mode shape appears with different orientation for different angles of attack in combination 1 & 2. The angles of attack have approximately the same value and opposite sign. They're also associated with approximately the same wind velocities. These plots show that the sign of α alone can have an influence on the mode shape orientation. Figure 6.23a has a larger lateral contribution than figure 6.23b, so higher α gives a larger lateral contribution in these cases.

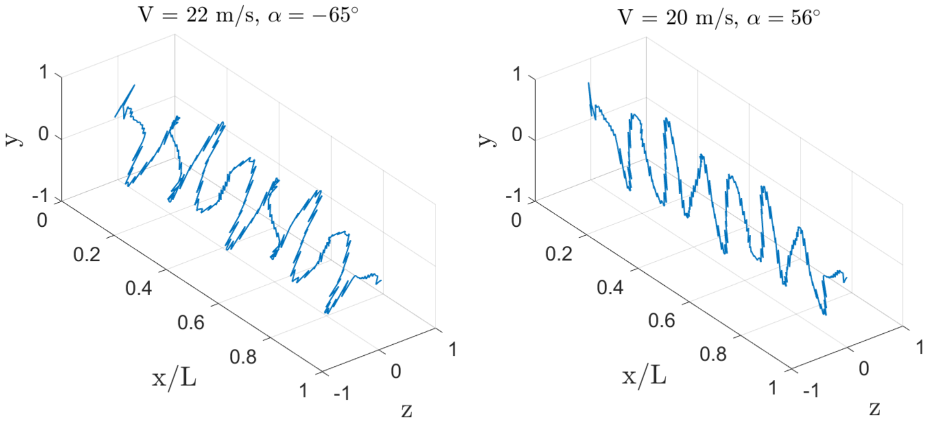

(a) V = 22 m/s, α= -65°.

(b) V = 20 m/s, α= 56°.

Figure 6.23: Same mode shape, different orientation at different α. For combination 1 & 2.

Combination 3 introduces a new lateral mode shown in figure 6.24. The shape fits still-air mode 48 which is dominant for the messenger wire. The displacement is smaller for the contact wire. The messenger wire, droppers and stitch wire is not included in the mode shapes shown in figure 6.21-6.24.

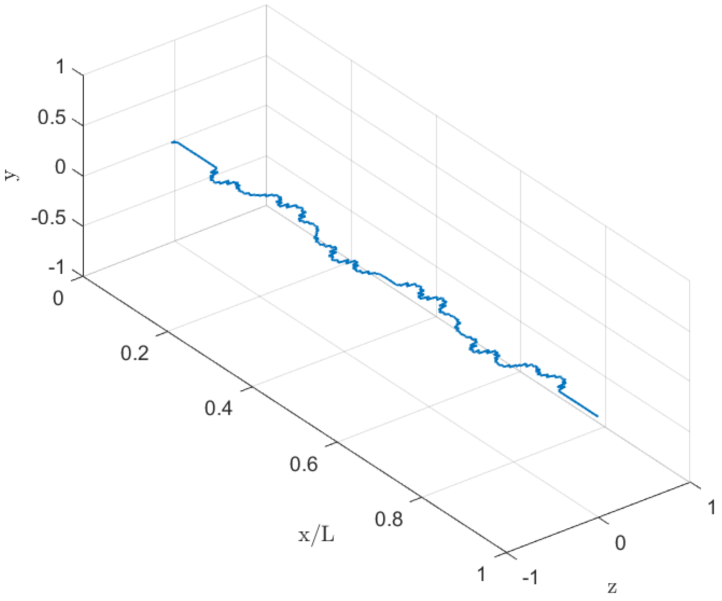

Figure 6.24: Mode shape, V = 20 m/s, α = -54, 48°. Combination 3. The mode shape is the same as still-air mode 48 in the FE-model.

The mode shapes denoted ”Vertical and lateral” in table6.3 were difficult to find in the still-air FE-model. Some were a fit in one direction only, others could possibly be a combination of two. Some were not found at all. It can be a challenge to compare modes when the polynomial eigenvalue modes are plotted for the contact wire while the FE-model includes the messenger wire, stitch wire and droppers. The aerodynamic stiffness and damping are not expected to change the still-air solution significantly. The off-diagonal terms contribute to changes, and these might be more significant for the α-V-combinations encountered here. A computer will probably be better at recognizing similarities. One example is shown in figure 6.25, where the vertical contribution is similar to still-air mode 37.

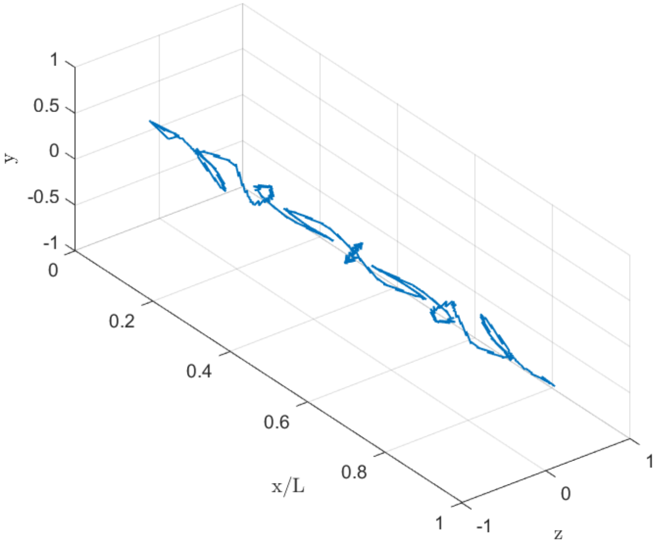

(a) 3D-plot

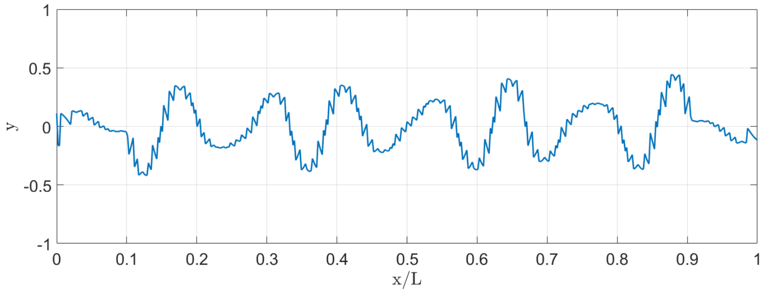

(b) Vertical contribution

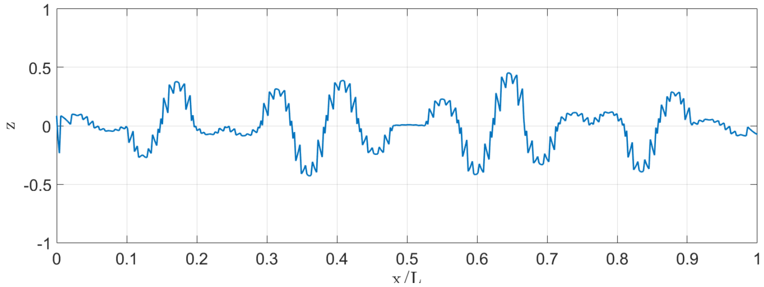

(c) Lateral contribution

Figure 6.25: Oblique mode shape. V = 20 m/s, α = 39°. V = 30 m/s, α = -60°.

The oblique mode shape shown in figure 6.26 appears four times for combination 3. A very similar shape is seen three times in combination 1 & 2.

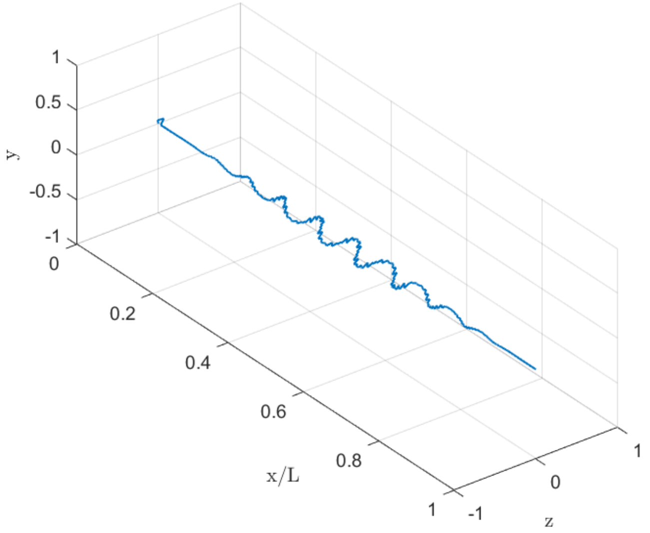

(a) 3D-plot

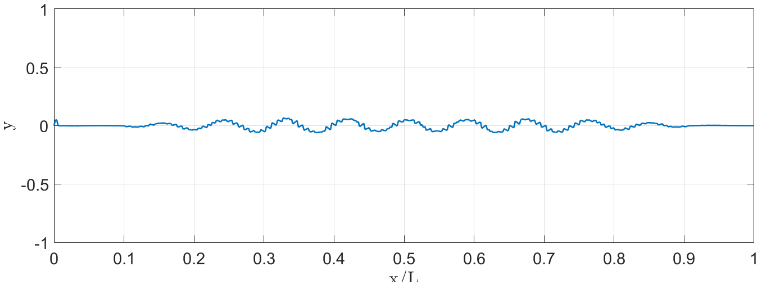

(b) Vertical contribution

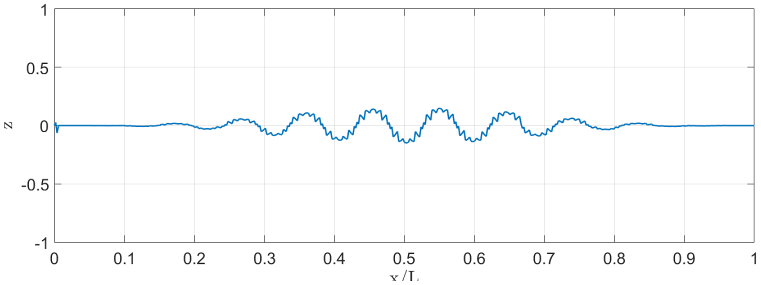

(c) Lateral contribution

Figure 6.26: Oblique mode shape. V = 30 m/s, α = -52, -51, 46°. V = 26 m/s, α = 46°.

6.5.2 Approach 2: Iterations with Criteria

The results presented for the second approach was obtained using the still-air modes described in combination 1. A certain number of still-air modes must be included to obtain results at all, for example including mode 1 to 10 doesn't yield any results. Including mode 1 to 20 yields results. Combination 1 includes a large span of modes without being to many. Including all 297 still-air modes would be very computationally expensive. The same analysis was performed at all angles of attack. The analysis checks for positive real(s). The critical value is found if real(s) is positive and less than CriteriaRe, and dV $<$ CriteriadV. If not, a velocity iteration is carried out. The iteration is different depending on if real(s) is positive or not.

Table 6.5 shows the results from an analysis with CriteriaRe = 0.01 and CriteriadV = 0.05. The analysis is performed with different wind velocity starting values. One can see that different start values, V_0, give different results. Some critical velocities aren't picked up when start value is low even though the iterations go through all integer V with dV = 1 (e.g. V_{CR} = 49.03125 m/s at $\alpha = 56°$). One reason for changing start values is that the measurements for the static coefficients at V = 20 m/s are not as trustworthy because measurements were taken during vortex shedding. The measurements at 6 m/s, corresponding to 30 m/s in real life, are more trustworthy. And the analysis is performed with V_0 = 31 m/s to exclude critical values below 30. V_0 = 30 m/s gave critical values of e.g. 29.03125 m/s. Still, as mentioned before, one can't with certainty exclude the lower critical values.

Table 6.6 shows the results from an analysis with CriteriaRe = 0.01 and no criteria for the velocity step. The analysis is performed with different wind velocity starting values. Also here it's evident that different start values, V_0, give different results. Some new angles of attack are introduced compared to table 6.5. E.g. α = -74, -57 and 25°. Some of the critical velocities are larger than in table 6.5, some critical velocities are lower. So the criterion for the velocity step is important for the determination of the critical velocity.

Table 6.5: Galloping analysis with CriteriaRe = 0.01 and CriteriadV = 0.05.

	V_{CR} [m/s]				
α [°]	V_0 = 20	V_0 = 25	V_0 = 31	V_0 = 40	V_0 = 50
-70	20.28125				
-68	20.03125				
-65	21.21875				
-64			31.03125		
-48	47	47	47	47	
15	25.09375	25.09375			
17	23.65625	24.03125			
19	28.3125	28.3125	30.03125		
20	26.71875	26.71875		39.03125	
21	27.28125	27.28125			
22	27.3125	27.3125			49.03125
23	25.6875	25.6875			49.03125
56					49.03125
59		24.03125	30.03125		

Table 6.6: Galloping analysis with CriteriaRe = 0.01, no CriteriadV

	V_{CR} [m/s]				
α	V_0 = 20	V_0 = 25	V_0 = 30	V_0 = 40	V_0 = 50
-74	20				
-70	20.5				
-68	20.5				
-65	21.5				
-64			30		
-57	20				
-48	47	47	47	47	
15	26	26			
17	24	24.5			
19	29	29	30		
20	27	27		40	
21	28	28			
22	28	28			50
23	26	26			50
25		25			
56	20				
59	20	25	30		50

Table 6.7 shows galloping analysis with different criteria for the real part of the eigenvalue, i.e. the criteria for damping. One can see that increasing the criteria for the damping includes more unstable angles and velocities. The goal of the analysis is to determine critical characteristics, and the onset of galloping happens when the damping goes from a negative to a positive value, i.e. when the damping is equal to zero. So a strict CriteriaRe with value as close to zero as possible is desirable. It's also important to not be too strict with the criterion, in order to discover possible instabilities. So checking for different criteria is important because it might introduce new critical angles and velocities not found otherwise. One can see from table 6.7 that most angles introduced with increasing CriteriaRe are already discovered. The exceptions are the instabilities at $\alpha = -72°$ and $\alpha = 16°$. The instabilites at angles of attack $\alpha = 15°, 17°, 20° - 23°$ and $\alpha = 56°$ are discovered at lower critical velocities. But the critical velocities larger than 30 m/s might be important because the WT-data is more trustworthy at V $>$ 30 m/s, as mentioned above.

Table 6.7: Galloping analysis with CriteriadV = 0.05 and different CriteriaRe, V_0 = 31 m/s.

CriteriaRe = 0.01		CriteriaRe = 0.05		CriteriaRe = 0.1	
α	V_{CR}	α	V_{CR}	α	V_{CR}
-64	30.03125	-64	30.03125	-72	30.03125
-48	47	-48	47	-64	30.03125
19	30.03125	15	30.03125	-48	47
59	30.03125	19	30.03125	15	30.03125
		20	30.03125	16	30.03125
		21	30.03125	17	30.03125
		22	30.03125	19	30.03125
		23	30.03125	20	30.03125
		59	30.03125	21	30.03125
				22	30.03125
				23	30.03125
				56	30.03125
				59	30.03125

Challenges with plotting mode shapes

One of the challenges with plotting mode shapes is choosing what still-air modes to include in the calculation. The transformation from the polynomial eigenvalue solution to the final mode shape plot is done with a coordinate transformation applying the still-air mode shapes. So, the final result should be strongly influenced by the choice. Two alternatives are discussed:

- Alternative 1: Still air mode 1, 2, 4, 7, 10, 11, 16, 17, 23, 24, 30, 31, 32, 40, 45, 47, 51, 53, 55, 58, 59, 60, 62, 65 and 70
- Alternative 2: All 297 still-air modes

The galloping analysis to find critical values was done including random still-air modes depicted in alternative 1. There are 297 still-air modes in total, and using all of them is alternative 2. The galloping analysis did not include all of them because the calculations would take a long time. But plotting the mode shapes takes less time which means that more modes can be included. The challenge with this is that including different number of still-air modes yields different mode shapes. One example is for $V_{CR} = 20.2813\ m/s$ at $\alpha = -70°$ shown in figure 6.27. When using the same modes as in the calculation (a few random still-air modes) the mode shape is dominant in the vertical direction (fig.6.27a). This contradicts the assumption that a high angle of attack gives a larger lateral contribution. But when the mode shape is plotted including all 297 still-air modes, the mode shape is more oblique with lateral and vertical contributions (fig.6.27b). The opposite is observed for $V_{CR} = 30.03125\ m/s$ at $\alpha = -72°$ (fig.6.29).

The vertical and lateral contributions of the mode shape including all still-air modes is shown in figure 6.28. The difference in plotted mode shapes might be because the randomly selected still-air modes don't include the matching lateral modes to represent the lateral contribution completely.

Table 6.8 shows the mode shapes associated with the lowest critical velocities determined, i.e. the onset galloping mode shapes. Some angles of attack are linked to two different critical velocities; one velocity below 30 m/s and one velocity greater than 30 m/s. The reason for this is, as mentioned before, is the trustworthiness of the wind tunnel results.

Depending on usage of alternative 1 or 2 one can see that the negative α's are associated with mode shapes with both lateral and vertical contributions. The α's ”closer” to zero and with greater positive values are associated to vertical mode shapes, with smaller lateral contributions. The grooves contribute to the flow around the cross-section. A negative and a positive angle of attack present very different surfaces to the wind flow. A large negative angle of attack puts the top of the contact wire cross-section, and therefore also the grooves, in the middle of the surface facing the flow (fig.4.7a). A large negative angle of attack ”hides” the top and grooves from the oncoming flow (fig.4.7f). Also, as mentioned before, the support poles and the other catenary wires suppress movement in certain directions.

Table 6.8: Mode shapes at the lowest critical velocities, calculated using alternative 1 or 2.

		Mode shape description	
α	V_{CR}	Alt.1	Alt.2
-74	20	Vertical	Vertical
-72	30.03125	Both vertical and lateral	Mostly vertical
-70	20.28125	Vertical	Both vertical and lateral
-68	20.03125	Vertical	Both vertical and lateral
-65	21.21875	Identical	
-64	30	Vertical	Vertical, small lateral
	31.03125	Vertical	Mostly vertical
-57	20	Vertical	Vertical
-48	47	Both vertical and lateral	Both vertical and lateral
15	25.09375	Identical	
	30.03125	Identical	
16	30.03125	Vertical	Vertical
17	23.65625	Identical	
	30.03125	Vertical	Mostly vertical
19	28.3125	Identical	
	30	Vertical, small lateral	Vertical, small lateral
20	26.71875	Identical	
	30.03125	Vertical	Mostly vertical
21	27.28125	Identical	
	30.03125	Vertical, small lateral	Vertical, small lateral
22	27.3125	Identical	
	30.03125	Vertical, small lateral	Vertical
23	25.6875	Identical	
	30.03125	Vertical	Vertical, small lateral
25	25	Vertical, small lateral	Mostly vertical
56	20	Vertical	Vertical, small lateral
	30.03125	Vertical	Vertical
59	20	Vertical, very small lateral	Vertical, small lateral
	30	Vertical, small lateral	Vertical, small lateral

No new angles of attack are introduced compared to approach 1. But some angles of attack exhibit larger critical velocities. E.g. at α = -64° the lowest critical velocity found is 30 m/s. All angles of attack, except for α = -48°, satisfy the Glauert-Den Hartog stability criterion. Approach 2 leads to a decrease in many of the critical velocities from approach 1, since velocity iterations with smaller time steps are used.

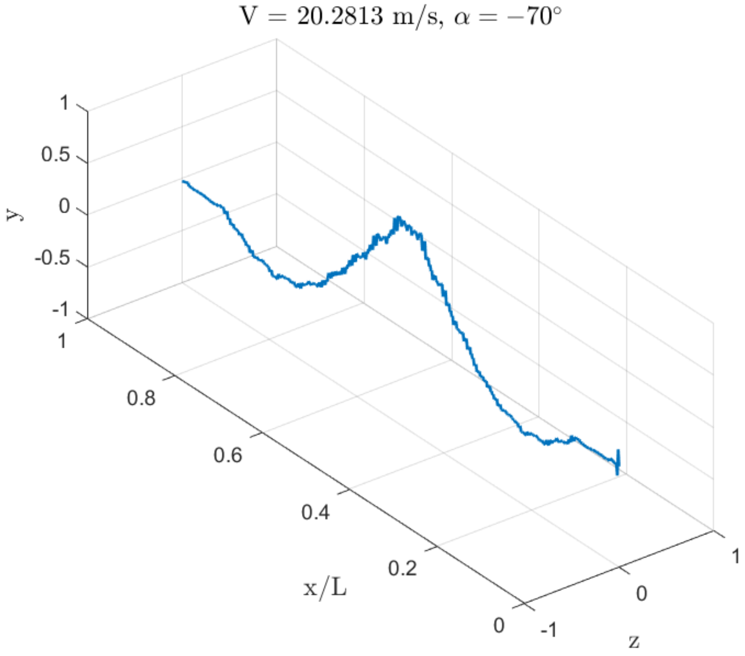

(a) Alternative 1.

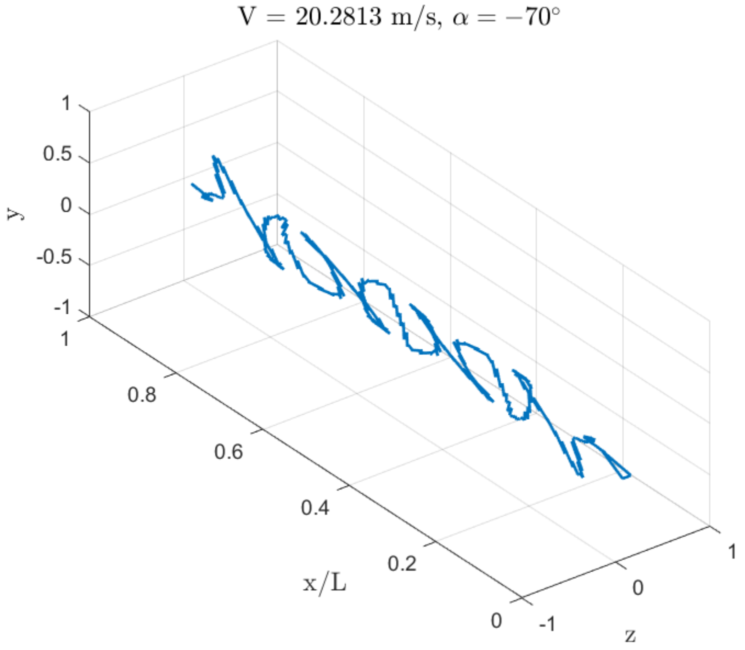

(b) Alternative 2.

Figure 6.27: Onset galloping mode shape at $V_{CR} = 20.2813\ m/s$ and $\alpha = -70°$.

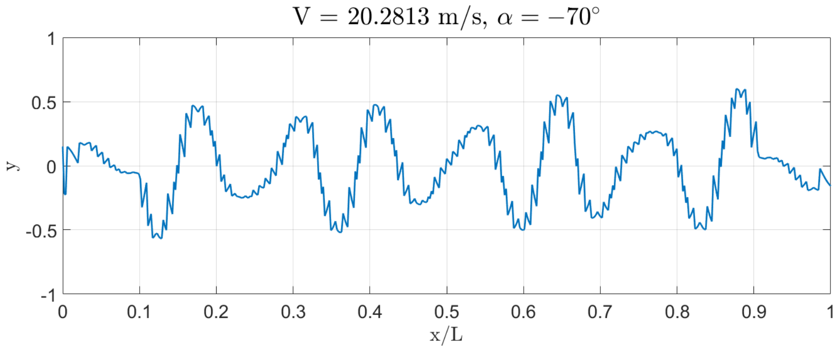

(a) Vertical mode shape

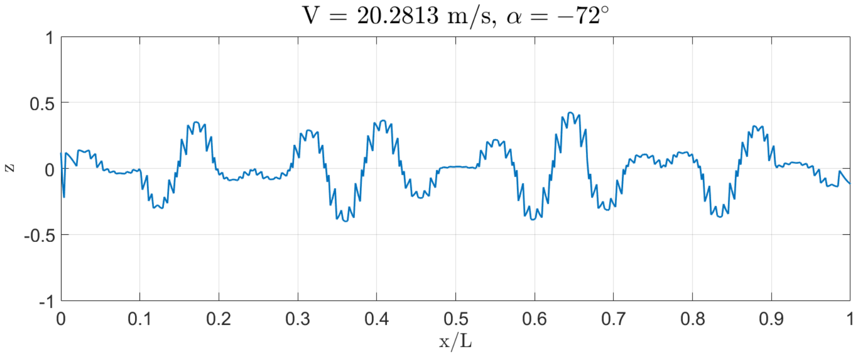

(b) Lateral mode shape

Figure 6.28: Onset galloping mode shape at $V_{CR} = 20.2813\ m/s$ and $\alpha = -70°$ ans using alternative 2.

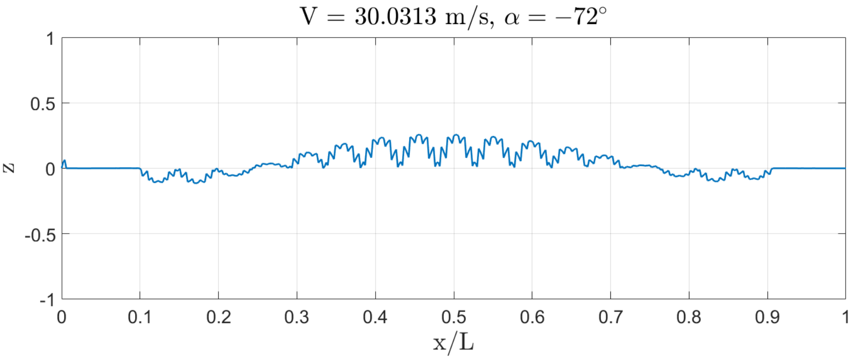

(a) Alternative 1.

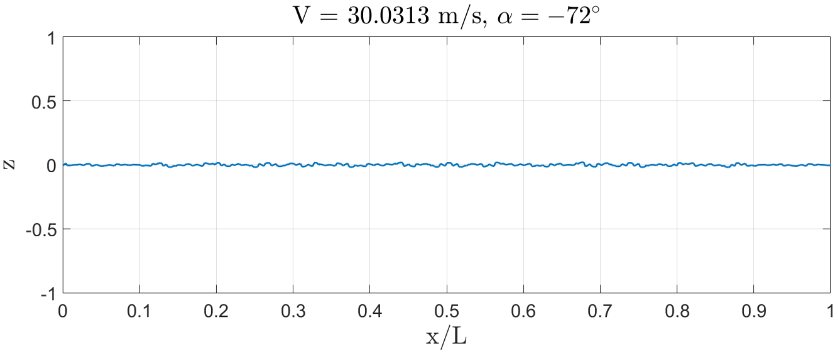

(b) Alternative 2.

Figure 6.29: Onset galloping lateral mode shape at $V_{CR} = 30.03125\ m/s$ and $\alpha = -72°$.

Chapter 7

Conclusion

This report carried out a wind tunnel test on an upscaled contact wire. Angles of attack ranged from -75 to 75°. Three wind velocities were tested; 4, 6 and 10 m/s. The results were plotted in the form of static aerodynamic coefficients versus angle of attack and Reynolds number. The results were also presented in the form of the Glauert-Den Hartog stability criterion for galloping. The Strouhal number was determined. The static coefficients were used to investigate galloping instabilities on a FE-model of a real life Norwegian railway stretch.

The static coefficients were dependent on Reynolds number and angle of attack. The drag coefficient decreased with increasing velocity. This was also evident in the plot versus Reynolds number, for α = 0. Minimum drag was for a flow angle of attack equal to approximately 50°. Maximum drag was for angles of attack between α's between -65 and -50°. The magnitude of the lift coefficient generally increased with increasing velocity. This is also seen in the plot versus Reynolds number. The sign of the flow angle and the sign for the lift coefficient were mostly the same. The moment coefficient increased with increasing velocity for negative angles of attack and decreased for increasing velocity at positive angles of attack. The plot against Reynolds number showed a decrease in the lift coefficient for increasing velocity.

The Glauert-Den Hartog stability criterion gives possible instabilities for all wind tunnel velocities. The criterion experiences the largest amount of negative values for wind tunnel velocity V = 4 m/s, a bit less for 6 m/s and the least amount of negative values for V = 10 m/s. The possibly unstable angles of attack range from about -74 to -57°, at some angles close to zero (only for V = 4 m/s), at some angles from 16 to 26°, and lastly for some angles from 55 to 64°.

The Strouhal number was determined from a time series with wind velocities from zero to 10 m/s. The mean Strouhal number from three calculations was 0.194. This value is close to that of a cylinder.

The galloping analysis was performed at all angles of attack from -75 to 75°. It provided many critical velocities at multiple angles of attack. The first approach plotted the real part of the eigenvalue at velocities from 20 to 50 m/s, to determine when the damping becomes positive. Many of the instabilities had critical velocities at 20 m/s. Some in between 20 and 30 m/s. Only one instability had a critical velocity above 30 m/s. Mode shapes were made for all critical velocities, and also for V = 30 m/s for some angles of attack, because of vortex shedding during wind tunnel testing. Most mode shapes were vertical at both low and high angles of attack. Some mode shapes showed vertical and lateral contributions at higher angles of attack. The aim of the second approach was to determine critical values for onset of galloping. No new critical angles of attack were introduced compared to approach 1. Many critical velocities were reduced as a result of a smaller velocity step.

Both the critical angle of attack and the critical velocity must occur at the same time for galloping to happen. So, although many critical values are found, galloping may still not occur. It may also not occur even if the critical values are present. Some angles of attack might not be probable to pair with some velocities. Galloping instabilities on catenary systems have not been recorded in Norway. The Glauert-Den Hartog criterion must also be satisfied for galloping to occur, and this excludes some of the critical values found in approach 1 combination 3.

One of the main limitations of the project is the vortex shedding at wind tunnel velocity 4 m/s. The measurements create many uncertainties in the galloping analysis. Another is that some of the galloping analyses performed include the messenger wire, droppers and stitch wire which are assigned the same static coefficients as the contact wire. This is of course not correct coefficients for these cross-sections.

Recommendations for further work:

- Short term:
  - Perform the second approach of the galloping analysis with even more still-air modes, and/or other combinations of modes.
  - Plot some of the mode shapes for sections instead of for the whole model. To avoid distorted mode shapes and to better understand the physical shape.
  - Investigate what realistic angles of attack are.
- Medium term:
  - When determining the Strouhal number, run the wind tunnel from 0 to 10 m/s with longer intervals of constant velocity. E.g. increase velocity a little bit, run at constant velocity for a while, increase velocity again, run that velocity for a while, and so on.
- Long term:
  - Find a model scaling that can be tested at WT-velocities corresponding to real-life velocities below 30 m/s without vortex shedding.

- Make alterations to the model to simulate effects like wear or ice build up. It's necessary to make a larger cross-section to simulate wear on the bottom of the contact wire. The distance from the aluminum pipe to the surface is to small on the current model.

Bibliography

Ammann, W. J., Natke, H. G., Nussbaumer, H., Pretlove, A. J., Rainer, J. H., 2011. Vibration Problems in Structures. Birkhäuser Basel.
URL `http://www.ebook.de/de/product/19297684/walter_j_ammann_hans_g_natke_hans_nussbaumer_anthony_j_pretlove_johann_h_rainer_vibration_problems_in_structures.html`

Cengel, Y. A., Cimbala, J. M., 2006. Fluid Mechanics: Fundamentals and Applications. Boston: McGraw-HillHigher Education.

Dowell, E. H., 2014. A Modern Course in Aeroelasticity. Springer International Publishing.
URL `http://www.ebook.de/de/product/25037937/earl_dowell_earl_h_dowell_a_modern_course_in_aeroelasticity.html`

Flamand, O., jul 1995. Rain-wind induced vibration of cables. Journal of Wind Engineering and Industrial Aerodynamics 57 (2-3), 353–362.

Gay, D., Gambelin, J., 2008. Modeling and Dimensioning of Structures: An Introduction. ISTE LTD.
URL `http://www.ebook.de/de/product/7498545/daniel_gay_jacques_gambelin_modeling_and_dimensioning_of_structures_an_introduction.html`

Gurit, n.d. Datasheet / gurit® pvc - structural foam core (v9). Web page.
URL `http://www.gurit.com/Our-Business/Composite-Materials/Structural-Core-Materials/Gurit-PVC`

Heyun, L., Xiaosong, G., Wenbi, T., mar 2012. Icing and anti-icing of railway contact wires. In: Reliability and Safety in Railway. InTech.

Jernbaneverket, 2012. Slik fungerer jernbanen. Web page.
URL `http://www.banenor.no/Jernbanen/Jernbanedrift---eit-komplisert-samspel/`

Kaczinski, M. R., 1998. Fatigue-resistant design of cantilevered signal, sign and light supports (NCHRP report). National Academy Press.

Newland, D. E., 2005. An Introduction to Random Vibrations, Spectral & Wavelet Analysis: Third Edition. DOVER PUBN INC.
URL `http://www.ebook.de/de/product/3100727/d_e_newland_an_introduction_to_random_vibrations_spectral_wavelet_analysis_third_edition.html`

NRK, MET Norway, 2013. Vindpiler og -skala. Web page.
URL `http://om.yr.no/symbol/vind/`

Song, Y., Liu, Z., Duan, F., Lu, X., Wang, H., 2018. Study on wind-induced vibration behavior of railway catenary in spatial stochastic wind field based on nonlinear finite element procedure. Journal of Vibration and Acoustics Vol. 140.

Stickland, M. T., Scanlon, T. J., 2001. An investigation into the aerodynamic characteristics of catenary contact wires in a cross-wind. Proc Instn Mech Engrs Vol 215 Part F, 311–318.

Stickland, M. T., Scanlon, T. J., Craighead, I. A., Fernandez, J., 2003. An investigation into the mechanical damping characteristics of catenary contact wires and their effect on aerodynamic galloping instability. Proc. Instn Mech. Engrs Vol. 217 Part F: J. Rail and Rapid Transit, 63–71.

Strømmen, E., 2010. Theory of Bridge Aerodynamics, 2nd Edition. Springer.

Tamura, Y., Kareem, A. (Eds.), 2013. Advanced Structural Wind Engineering. Springer Japan.

Xie, Q., Wang, W., Zhang, H., Zhi, X., 2014. Wind tunnel test on aerodynamic force characteristics of ice coating contact wire for high speed railway. China Railway Science Vol. 35 No.1.

Appendix

Appendix A

Acronyms

CW Contact wire

DFT Discrete Fourier transform

FFT Fast Fourier transform

MW Messenger wire

ST Stitch wire

WT Wind tunnel

Appendix B

Mode Shape Details

Table B.1 shows the mode shape details for the first approach of the galloping analysis. The results are for combination 1 & 2.

Table B.1: Mode shapes from galloping approach 1, and matching with still-air modes from the FE-model. Combination 1 and 2.

α [°]	V$_{CR}$ [m/s]	f$_{CR}$ [Hz]	FE mode	f$_{FE}$ [Hz]
-74	20	0.8765	8	0.87679
-72	20	2.1807	103	2.1806
	30	3.4177	192	3.4117
-71	30	1.4993	y: 51, z: 63	y1.4372 , z1.4865
	20	4.8289	y: 270	4.8291
-70	21	0.9649	y: 11, z: 14	y0.96465 , z0.99896
	30	1.4864	61/62	1.4833/1.4837
-69	20	1.1126	41	1.1129
	30	1.4499	difficult, 53	1.4359
-68	20	0.7629	1	0.76272
	30	1.0103	difficult, z: 29	1.0388
-67	30	1.4474	difficult, 52/53	1.4431/1.4508
	20	3.1782	179/180	3.1712/3.1779
-65	22	1.028	difficult, y: 19, z: 25	y1.0311, z1.0371
	30	3.8806	210	3.8947
-64	30	1.0302	19	1.0311
	20	1.6601	70	1.6601
-63	20	3.2282	182	3.2277
-62	20	4.6232	262	4.6234
-60	20	1.7096	71	1.7096
-57	20	0.9992	14	0.99896
15	25	0.7628	1	0.76272
	30	2.2481	106	2.248

16	30	3.1777	179/180	3.1712/3.1779
	20	4.1079	242	4.1081
17	24	0.8372	6	0.83714
	30	2.6477	129	2.6478
19	28	0.7628	1	0.76272
	30	1.114	42	1.1139
20	27	0.8143	5	0.81419
	30	1.8571	74	1.857
21	28	0.8769	8	0.87679
	30	1.4637	55	1.4636
21	30	2.2062	105	2.2061
	28	0.8769	8	0.87679
22	30	1.5303	67	1.5302
23	26	0.8143	5	0.81419
25	20	1.4912	64	1.4909
55	20	1.5684	68	1.5684
56	20	1.032	y: 19	y1.0311,
	30	2.7205	133	2.7201
57	30	1.4968	difficult, z: 63	z1.4865
	20	4.0481	236	4.0482
58	30	1.5022	difficult, z: 63	z1.4865
	20	2.0791	101	2.0792
59	20	0.877	8	0.87679
	30	0.877	8	0.87679

Table B.2 shows the mode shape details for the first approach of the galloping analysis. The results are for combination 3.

Table B.2: Mode shapes from galloping approach 1, and matching with still-air modes from the FE-model. Combination 3.

α [°]	V$_{CR}$ [m/s]	f$_{CR}$ [Hz]	FE mode	f$_{FE}$ [Hz]
-73	20	0.7628	1	0.76272
-72	20	2.1807	103	2.1806
-70	20	1.0343	19	1.0311
	30	1.4864	61/62, 65/66	1.4833/1.4837, 1.5080/1.5100
-69	20	1.1126	41	1.1129
	30	1.4499	difficult, 53	1.4359
-68	20	0.7629	1	0.76272
	30	1.0103	difficult, z: 29	1.0388
-67	30	1.4474	difficult, 52/53	1.4431/1.4508
	20	3.1782	179/180	3.1712/3.1779
-65	20	0.7625	1	0.76272
	30	3.8806	210	3.8947
-64	30	1.0302	19	1.0311

	20	1.6601	70	1.6601
-62	30	0.7627	1	0.76272
	22	3.9903	233	3.9903
-61	30	0.7627	1	0.76272
	20	1.4837	61/62	1.4833/1.4837
-60	30	1.0587	difficult, y: 37	1.0577
	20	1.7096	71	1.7096
-59	20	1.4841	61/62	1.4833/1.4837
	30	1.4865	61/62	1.4833/1.4837
-58	20	1.4838	61/62	1.4833/1.4837
	30	1.4945	61/62	1.4833/1.4837
-57	20	0.9992	14	0.99896
-56	30	1.0508	difficult, y: 37	1.0577
	20	1.486	61/62	1.4833/1.4837
-55	20	1.4837	61/62	1.4833/1.4837
	30	1.4923	61/62	1.4833/1.4837
-54	20	1.4209	48	1.4253
	30	1.4962	61/62	1.4833/1.4837
-52	30	1.4745	difficult, z: 63	1.4865
	22	1.4815	61/62	1.4833/1.4837
-51	30	1.4799	difficult, z: 63	1.4865
	20	1.4849	61/62	1.4833/1.4837
-50	20	0.7621	1	0.76272
-49	20	0.7621	1	0.76272
-48	20	1.484	61/62	1.4833/1.4837
-46	20	1.484	61/62	1.4833/1.4837
-43	20	0.7626	1	0.76272
-34	46	1.4824	61/62	1.4833/1.4837
16	20	4.1079	242	4.1081
20	20	0.7626	1	0.76272
38	30	1.4836	61/62	1.4833/1.4837
	25	1.4838	61/62	1.4833/1.4837
39	20	1.0533	difficult, z: 32 , y: 37	z1.0395, y1.0577
	30	1.4799	61/62	1.4833/1.4837
40	24	1.4824	61/62	1.4833/1.4837
	30	1.4824	61/62	1.4833/1.4837
42	30	1.4818	61/62	1.4833/1.4837
	29	1.4825	61/62	1.4833/1.4837
43	30	1.4811	61/62	1.4833/1.4837
	27	1.4825	61/62	1.4833/1.4837
44	30	1.4789	61/62	1.4833/1.4837
	28	1.4811	61/62	1.4833/1.4837
45	28	1.4818	61/62	1.4833/1.4837
	30	1.4831	61/62	1.4833/1.4837
46	26	1.4759	difficult, 63	1.4865

	30	1.4807	difficult, 63	1.4865
48	20	1.4206	48	1.4253
	30	1.4791	61/62	1.4833/1.4837
59	46	1.5186	difficult, z: 60, y: 55	y1.4636, z1.4832